Lab on a Chip

ROYAL SOCIETY OF CHEMISTRY

CRITICAL REVIEW

View Article Online
View Journal | View Issue

Cite this: *Lab Chip*, 2023, **23**, 1011

Optofluidic imaging meets deep learning: from merging to emerging

Dickson M. D. Siu, [a] Kelvin C. M. Lee, [a] Bob M. F. Chung,[b] Justin S. J. Wong, [c] Guoan Zheng[d] and Kevin K. Tsia *[ab]

Received 31st August 2022,
Accepted 22nd November 2022

DOI: 10.1039/d2lc00813k

rsc.li/loc

Propelled by the striking advances in optical microscopy and deep learning (DL), the role of imaging in lab-on-a-chip has dramatically been transformed from a silo inspection tool to a quantitative "smart" engine. A suite of advanced optical microscopes now enables imaging over a range of spatial scales (from molecules to organisms) and temporal window (from microseconds to hours). On the other hand, the staggering diversity of DL algorithms has revolutionized image processing and analysis at the scale and complexity that were once inconceivable. Recognizing these exciting but overwhelming developments, we provide a timely review of their latest trends in the context of lab-on-a-chip imaging, or coined optofluidic imaging. More importantly, here we discuss the strengths and caveats of how to adopt, reinvent, and integrate these imaging techniques and DL algorithms in order to tailor different lab-on-a-chip applications. In particular, we highlight three areas where the latest advances in lab-on-a-chip imaging and DL can form unique synergisms: image formation, image analytics and intelligent image-guided autonomous lab-on-a-chip. Despite the on-going challenges, we anticipate that they will represent the next frontiers in lab-on-a-chip imaging that will spearhead new capabilities in advancing analytical chemistry research, accelerating biological discovery, and empowering new intelligent clinical applications.

1. Introduction

The impact of microfluidics, ranging from analytical chemistry, single-cell biology, diagnostics, to pharmaceutics, has stretched far beyond the seminal vision of Manz *et al.* in the early 90s, coined 'miniaturized total chemical analysis systems' (μTAS)[1] or now broadly regarded as lab-on-a-chip. Notable examples include a host of technologies that transform single-cell omics analysis, large-scale drug screening, circulating tumor cell isolation, circulating DNA detection in blood,[2,3] among others – empowering sensitive personalized medicine.

Also fueling these applications is the continuous innovation in optical microscopy. Embracing the unspoken motto "seeing-is-believing", the microfluidics developers often incorporate imaging for sample monitoring, detection, and analysis in the lab-on-a-chip routine. Tremendous breakthroughs of high-resolution and high-speed microscopy have been made transferrable to the microfluidics community – leading to a new synergism between optical imaging and microfluidics, coined optofluidic imaging. Notably, a suite of emerging high-speed optical microscopy techniques is now available to tailor single-cell optofluidic imaging at the throughput not achievable in any available imaging flow cytometers.[4–6] Furthermore, these high-speed imaging tools also offer a wide range of imaging contrasts that reveal multifaceted traits of the microfluidic samples (including particles, cells, tissues, or even organisms), such as their biophysical/mechanical and biochemical signatures, even at the resolution beyond the classical diffraction limit.[7,8]

Speaking of imaging, one should not dismiss the advances of deep learning (DL) in the past decade. Not only has DL, notably convolutional neural networks (CNNs),[9,10] revolutionized the traditional image processing pipeline (*e.g.* image reconstruction, transformation and analytics), but has also incubated new computational microscopy modalities.[11] This stunning success enticed researchers to turn to DL strategies in the current optofluidic imaging development. Since its inception in 2014, the trend in adopting (deep) machine learning in optofluidic imaging has increased steadily and continues to hit its stride, consistently representing the majority of $\sim\frac{2}{3}$ in publication numbers in DL microfluidics (Fig. 1). Despite the growth, researchers should also be aware of the challenges and opportunities ahead. The

[a] *Department of Electrical and Electronic Engineering, The University of Hong Kong, Hong Kong, Hong Kong. E-mail: tsia@hku.hk*
[b] *Advanced Biomedical Instrumentation Centre, Hong Kong Science Park, Shatin, New Territories, Hong Kong*
[c] *Conzeb Limited, Hong Kong Science Park, Shatin, New Territories, Hong Kong*
[d] *Department of Biomedical Engineering, University of Connecticut, Storrs, CT, USA*

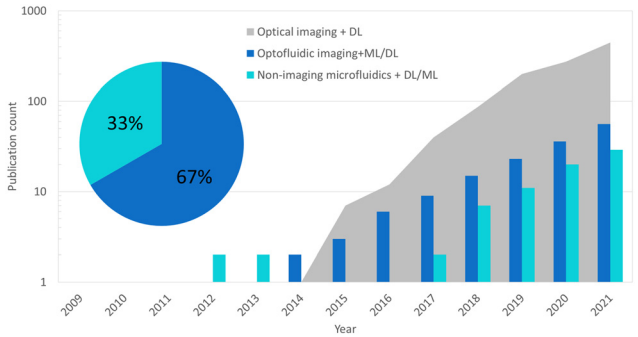

Fig. 1 Publication trend in the fields related to machine-learning (ML)/deep-learning (DL) and microscopy in the past decade. The data was extracted from the search engine of PubMed with the search keywords of "microfluidics", "imaging", "deep learning", and "machine learning" (between 2009 and 2021).

collection of DL imaging methods is expanding at a staggering rate that can be daunting for many microfluidics developers to adopt, not to mention the targeted users such as chemists, biologists and clinicians. On the other hand, current DL models for microscopy are not always well generalizable to diverse data captured from different modalities.[12,13] Hence, a simple "plug-and-play" approach that combines the existing DL tools with optofluidics imaging is often not trivial and even adds to difficulty. To this end, this article aims to highlight the advantages and caveats of the latest development of DL optofluidic imaging. Based on the recent progress, we identify three promising areas where optofluidic imaging and DL can find unique synergistic grounds that were once uncharted in microfluidics: (1) DL optofluidic image formation; (2) DL optofluidic image analytics; and (3) intelligent image-guided autonomous microfluidics. Obtaining a holistic understanding of these latest trends could help researchers

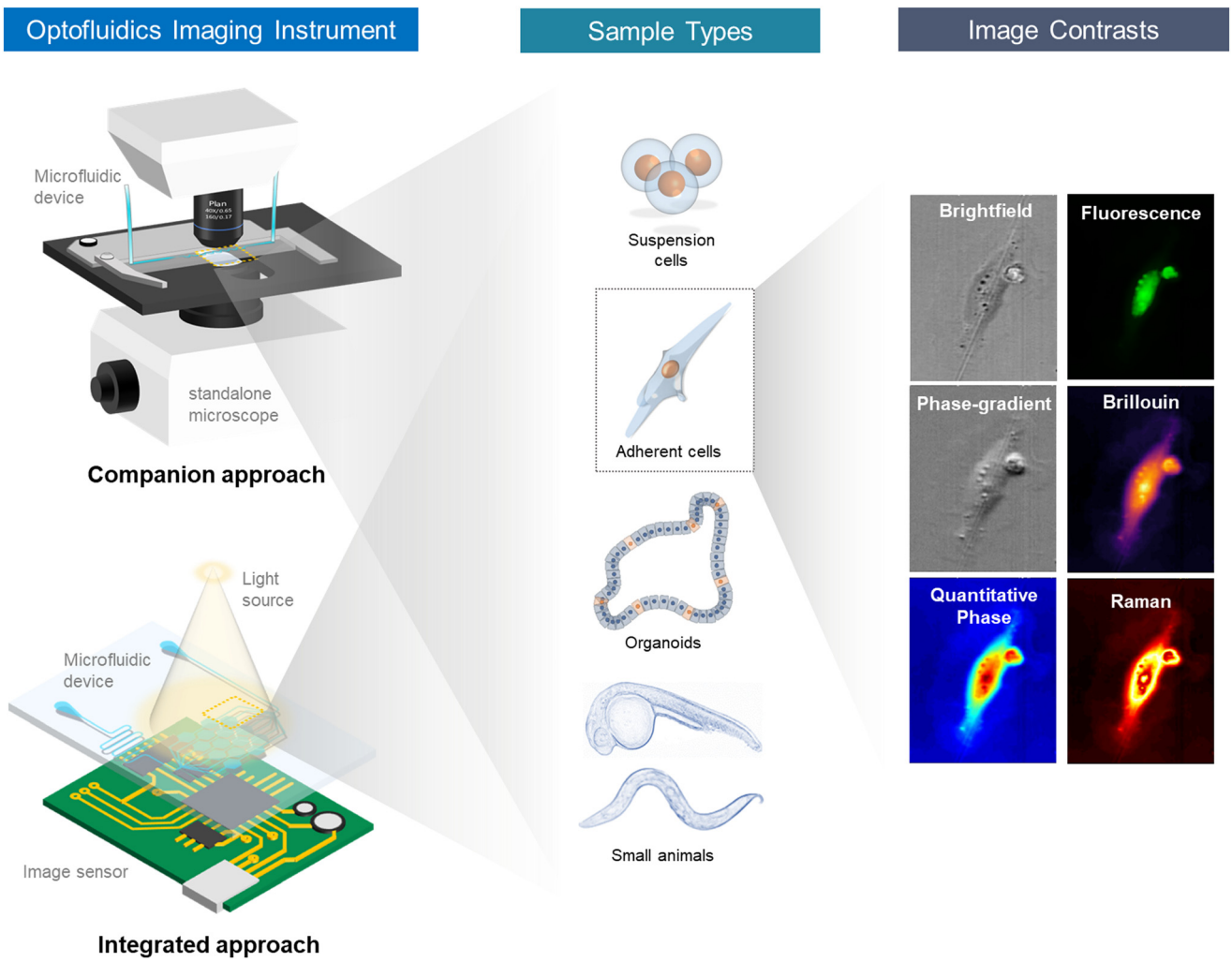

Fig. 2 (Left) General strategies of optofluidic imaging: companion and integrated approach. (Middle) Common sample types, especially in biological and biomedical applications. (Right) Available image contrasts, each of which reveals different traits of the samples. For instance, the biophysical/mechanical properties can be read out by bright-field, phase-gradient and quantitative phase image contrasts whereas biomolecular/biochemical signatures can be revealed by fluorescence imaging, vibrational imaging (*e.g.* Brillouin and Raman scattering).

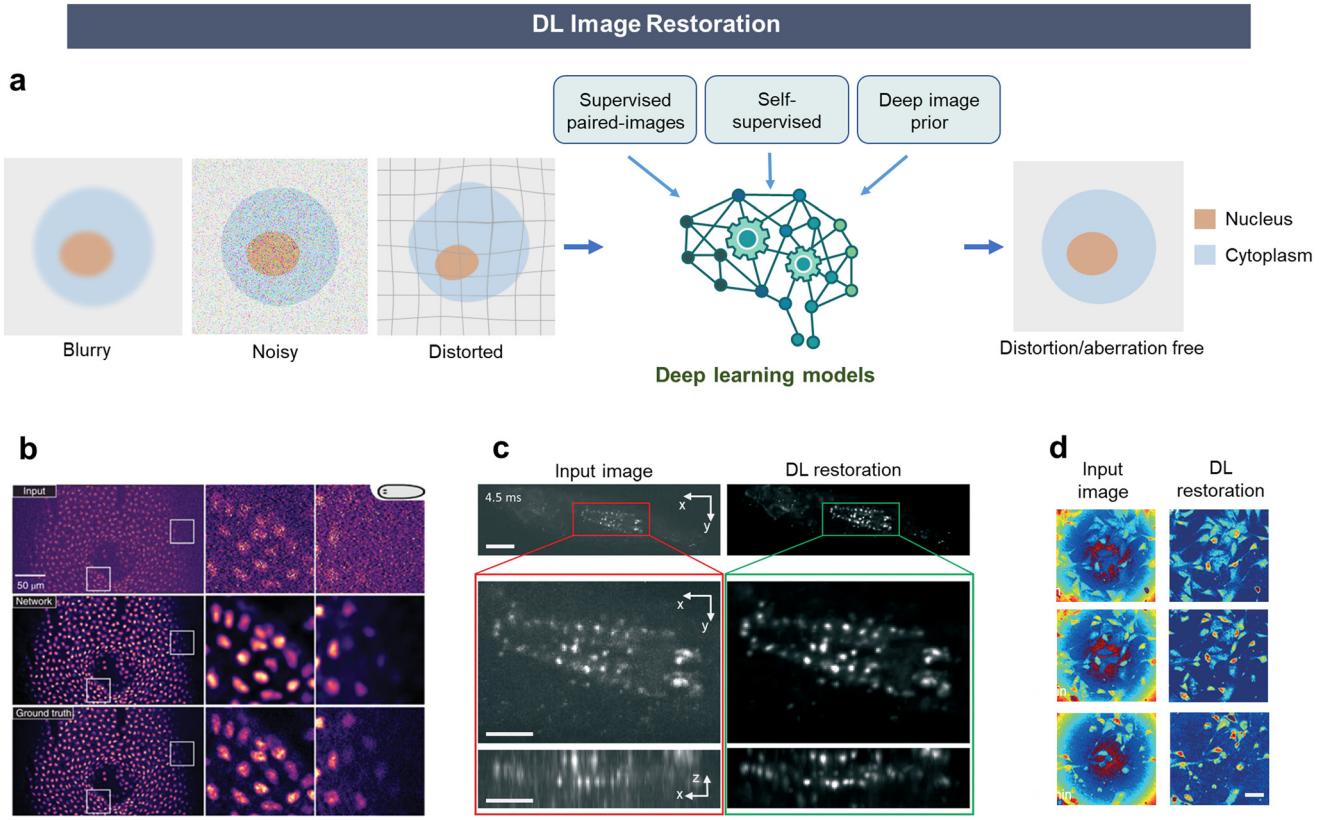

Fig. 3 (a) General principle of DL image restoration. (b) Example of denoising using content-aware image restoration (CARE) network, which successfully reduced photon exposure by 60-fold. The imaged object is a nucleus-stained flatworm (*S. mediterranea*). Reproduced from ref. 34 with permission from Springer Nature. (c) On-chip 3D light sheet imaging of a freely moving Drosophila larva. A deep neural network model was used for denoising and restoring isotropic resolution in 3D. Reproduced from ref. 23 with permission from Royal Society of Chemistry. (d) CNN-based phase aberration correction in a microfluidic shear stress system, where the adherent cells were imaged at different time points by digital holographic microscopy. Reproduced from ref. 40 with permission from Royal Society of Chemistry. Scale bars: (b) 10 μm, (c) 50 μm, and (d) 40 μm.

better identify the optimal strategies that incentivize new forms of integration of DL with optofluidic imaging, and thus redefine the unique role of DL in optofluidic imaging for advancing analytical assays and clinical applications.

2. Deep-learning optofluidic image formation

The state-of-the-art optofluidic imaging platforms generally follow two design strategies (Fig. 2): (1) a "*companion approach*" in which the microfluidic chip is positioned under a standalone advanced (or standard) microscope for image capture. (2) An "*Integrated approach*" in which the microfluidic chip is physically integrated with the microscope elements, including miniaturized optics and camera sensor.[14–16] In both approaches, the image quality can commonly be exacerbated by the microfluidic designs and operations, which do not normally appear in the standard microscopy settings. Examples include the image blur and loss of sensitivity due to fast microfluidic flow, and the compromised image quality due to aberrations introduced by the microfluidic materials and channel geometry. DL methods have been used as a data-driven statistical inference tool for achieving robust and high-quality image restoration, image reconstruction, and image augmentation. Note that these methods are now widely adaptable to the wide-ranging sample types including cells in suspension or adherent form, organoids and small animals. They can be applied to different imaging modalities, *e.g.* bright-field imaging, label-free quantitative phase microscopy, fluorescence imaging, and vibrational imaging *via* Raman[17–19] and Brillouin scattering[20,21] (Fig. 2). The applicability further extends to other advanced imaging modalities that have also tapped into microfluidics,[7,8,22] including light-sheet microscopy,[23–25] fluorescence lifetime imaging, single-molecule localization microscopy (SMLM),[26] and structured illumination (SIM).[27]

2.1 Deep-learning image restoration

Originally developed in computer vision, assorted DL image restoration methods, which outperform many classical restoration solutions, can now be tailored to combat the aberration problems in optofluidic imaging (Box 1) (Fig. 3a). DL image restoration can be regarded as a complex

Box 1 Image degradation in optofluidic imaging

The image quality in optofluidic imaging can be degraded by the aberration effects (*i.e.* image blur, distortion) induced by the imaging and the microfluidic systems, as well as the intrinsic noise from light sources and photodetector/image sensors. Typical image degradation examples include out-of-focus blur caused by non-ideal microfluidic focusing of suspension cells, motion blur due to the microfluidic flow[28] or rapid sample scanning, and optical wavefront distortion induced by the additional layer of the microfluidic channel or the imperfect optical components in the system. The problem of image noise is particularly relevant in biological microscopy. This is because low illumination intensities are required to ensure biological viability and physiological relevance of the effect monitored, resulting in weak light signals and limited image signal-to-noise (SNR). This situation is even more challenging in high-speed or high-throughput optofluidic imaging assays where the imaging exposure time has to be further reduced. Aberration can be minimized by specialized optical designs of compound lenses whereas noise issues can be partially mitigated using high-end sensitive cameras. However, such hardware systems inevitably increase the complexity and cost of the system. In view of light-weight, low-cost but high-quality optofluidic applications, computational approaches for correcting the aberration (called deconvolution) and combating the noise are more favorable.[29,30] Nevertheless, current methods struggle to be generalized to handle diverse aberration and noise models which are mostly system- and application-dependent. In particular, aberration and noise can be heterogeneous across the imaging field-of-view (FOV), and even varying in time.

mathematical operation that maps a low-quality (blurry/distorted/noisy) image to its high-quality counterpart. Such operation is mainly carried out by neural network models (predominantly in the form of CNN), and often involve millions of variables to be adjusted. The overarching task is to train a DL model such that it learns how to tune these variables based on training data, in order to improve the image quality at the model output. This training step is critical and is implemented in either a supervised or self-supervised manner.[9]

Supervised learning involves a straightforward training process which requires the paired (low-quality) input and (high-quality) output images. The model learns the specific transformation from the corrupted, low-quality input images to the output images with the desired quality. This learning strategy can also be applied to image reconstruction and augmentation as discussed later. Many different variants of the CNN architectures have been developed in order to tailor different imaging scenarios and improve the fidelity of the output images.[31,32] A residual network (ResNet) was used in deblurring the single-cell images in a high-throughput imaging flow cytometer.[33] Content-aware image restoration (CARE) networks[34] use the U-Net[35] (a popular CNN architecture) trained with a large dataset of noisy and paired high-quality images for denoising of fluorescence microscopy images, outperforming many standard denoising algorithms (Fig. 3b).

Self-supervised learning, on the other hand, does not require annotated paired training dataset and predicts high-quality output images by directly learning the implicit patterns in the input noisy image data. Self-supervised models can thus be easily adaptable to different imaging settings. In the context of denoising, it should be noted that these self-supervised models rely on a key assumption that the noise in an image is statistically independent for each pixel (*e.g.* Noise2Noise,[36] Noise2Void,[37] Noise2self[38]), which is often true in fluorescence microscopy.[39]

Many of these DL models (supervised or self-supervised) are not limited to performing one single image restoration task. For example, CARE and residual channel attention networks[41] can perform not only denoising, but also out-of-focus background removal and resolution enhancement. Image denoising can be combined with image deconvolution,[42] or image segmentation.[43] Likewise, a U-net architecture was designed for both denoising and axial resolution enhancement that enabled isotropic high-speed 3D light-sheet fluorescence microfluidic imaging of a whole Drosophila larva at single-cell resolution[23] (Fig. 3c). Another notable advancement is the use of generative DL models (notably generative adversarial network (GAN)[44]) for image restoration. Different variants of GAN-based models (*e.g.* CycleGAN.[45] Notably, Deep-Z[46,47]) have also been applied for deconvolution in optical microscopy. More recently, vision transformer networks are beginning to replace CNN for various vision tasks.[48] It has also been demonstrated in SIM for increasing the temporal resolution by almost 10 times.[49]

The data-driven nature of DL makes it versatile in obtaining system aberrations in different ways. CNN has been used as a regression model that quantifies the common patterns in the training image datasets contributed by the aberration and noise in microfluidic digital holographic imaging (Fig. 3d).[40] Also promising is an emergent class of "deep prior" methods that can effectively be adapted and generalized to real-world aberration scenarios (*e.g.* spatially variant aberrations[50,51] and noisy images[52]) without involving complete model retraining. Recently, a U-net model was paired with a Wiener-filter-based deconvolution method such that the prior (or regularization) of the deconvolution filter was made "learnable". Not only can it take into account the spatially variant aberration, but also offer more than 1000 times improvement in computation speed compared to the common iterative method.[51] This attribute is particularly attractive in high-speed and dynamical optofluidic imaging applications.

2.2 Deep-learning image reconstruction

In many imaging scenarios, the raw data recorded by image sensors/detectors only represents the incomplete or intermediate form of the imaged sample. Additional computational steps are needed to retrieve the target sample information otherwise hidden in the raw image recording. Examples include reconstructing the 3D cellular or whole organism information based on only a few or even a single 2D image acquisition, super-resolution cellular information

from incomplete low-resolution image acquisition,[53] and the retrieval of lost phase information from intensity measurements. On many occasions, *a priori* knowledge of how the sensor/detector and the rest of the optical system encode the sample information is needed, but very often unavailable, especially when it is mixed with noise. Hence, image reconstruction, which aims to inverse this encoding operation, is ill-posed. Although there are a plethora of analytical or iterative image reconstruction algorithms developed for different imaging modalities, especially tomographic imaging,[54] many of them still struggle to efficiently yield robust, well-defined solutions.

DL presents a data-driven approach that can learn the non-trivial inverse image transformation reconstruction with superior efficiency and fidelity. While DL image reconstruction methods have proven themselves broadly applicable in different imaging problems,[53] they have demonstrated distinctive advantages in enhancing the performance of optofluidic imaging capabilities, especially in achieving 3D and super-resolution microscopy, without complicating the imaging hardware. A notable example is lensless imaging which is particularly powerful in reducing the system form factor and thus maximizing the portability and scalability.[16,55]

2.2.1 3D image reconstruction. Beyond a doubt, the blossoming advances in 3D microscopy (*e.g.* confocal,[56] multiphoton,[57] light-sheet[58] microscopy) have incentivized 3D optofluidic imaging approaches, especially in 3D imaging

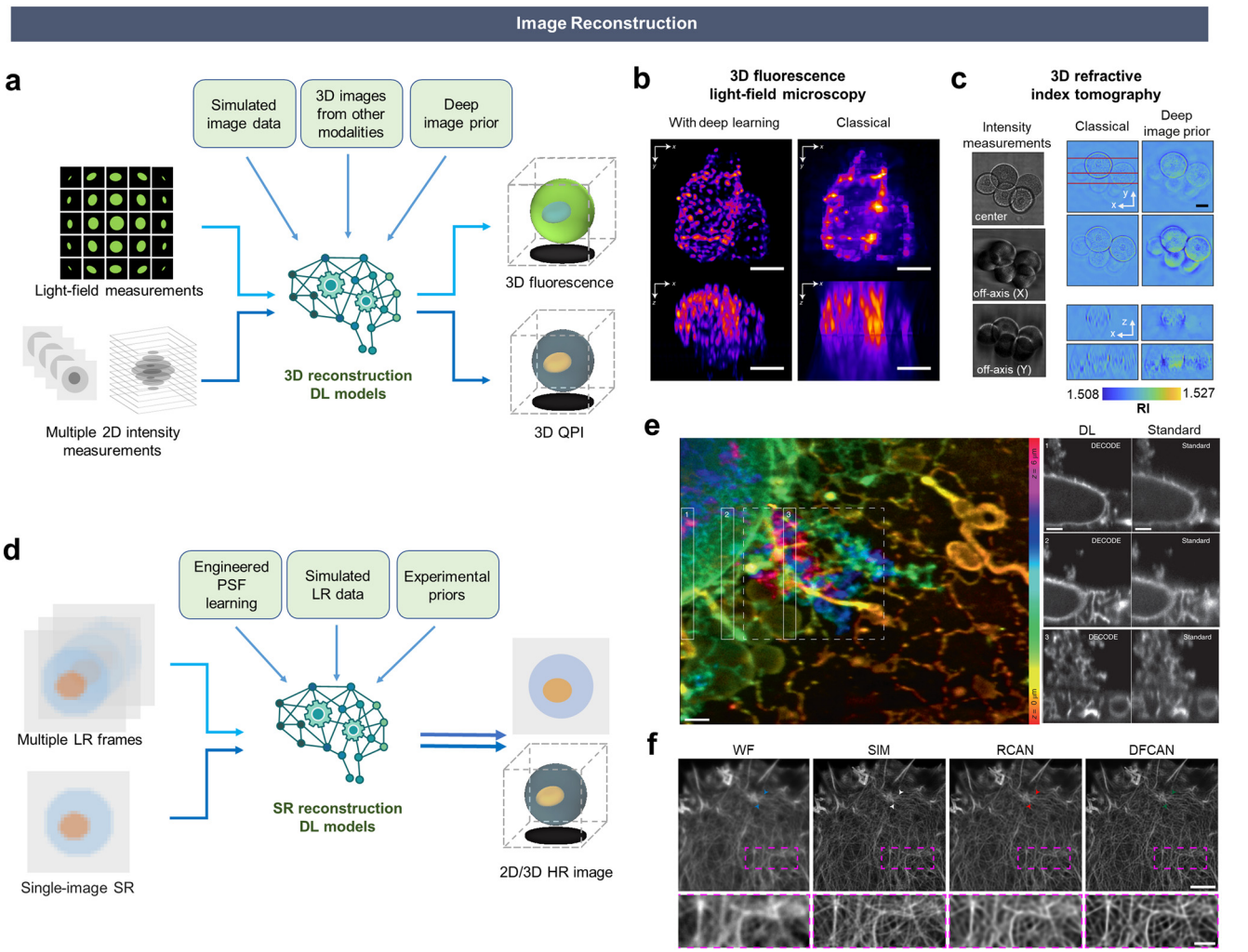

Fig. 4 (a) Common strategies of 3D image reconstruction by DL. (b) 3D fluorescence image reconstructed from the raw light-field measurement. Reproduced from ref. 85 with permission from Springer Nature. (c) 3D refractive index tomography by deep image prior. Reproduced from ref. 88 with permission from the Optica Publishing Group. (d) The general principle of SR image reconstruction by DL. (e) (Left) DL reconstruction in lattice light sheet imaging combined with the PAINT technique. (Right) Comparison of the axial reconstruction performance (between DL and standard maximum likelihood estimation method). The axial cross-sectional reconstructions cover the 500 nm-thick regions as indicated in the left panel. Reproduced from ref. 89 with permission from Springer Nature. (f) DL-based SISR image reconstruction (F-actins) by deep Fourier channel attention network DFCAN and deep residual channel attention network RCAN. Wide-field (WF) and ground-truth SIM (GT-SIM) images are displayed for reference. Boxed regions in the upper images are magnified and displayed in the lower row. Reproduced from ref. 90 with permission from the Optica Publishing Group. Scale bars: (b) 50 μm, (c) 10 μm, (e) 1 μm and (f) 3 μm (1 μm for magnified images).

flow cytometry,[24,59–62] on-chip 3D microtissues imaging,[63,64] and animal (zebrafish larvae and embryos) imaging.[65] However, these advanced techniques still face the key challenge of maximizing the following attributes at the same time: high-resolution in all three dimensions, a large FOV in 3D, low risk of phototoxicity/photobleaching, and high imaging speed. For example, the majority of 3D imaging strategies rely on scanning illumination/detection mechanisms to densely record many image planes to stack a 3D object with high axial resolution. This process however significantly slows down the imaging speed, not to mention the risk of inducing out-of-focus phototoxicity and photobleaching effect.[66] In lab-on-a-chip applications, achieving high-speed and/or high-throughput live-cell 3D imaging is even more challenging as cells often flow in suspension at high-speed, or the organisms/animals are allowed to freely move within the micro-channels/-chambers/-wells.

Conventional methods for 3D image reconstruction, especially those involving phase retrieval (Box 2), are generally ill-posed, computationally demanding, and significantly susceptible to noise. In contrast, DL-based holographic[80–82] or ptychographic[83] image reconstruction (quantitative recovery of phase and amplitude of the image) can obtain similar results as the regular model-based algorithms by adopting a supervised end-to-end training strategy. Nevertheless, these methods require a large amount and/or precisely-calibrated experimental ("ground-truth") training data that are commonly lacking or even unavailable in many imaging settings. In order to maintain the robustness and generalizability of the DL networks, one solution is to generate synthetic (simulated) data based on the image formation/transformation model (Fig. 4a).[84] For example, using a wave-optics model, Wang *et al.* demonstrated DL-based 3D light-field microscopy based on transforming the available high-resolution 3D images into 2D light-field images for paired data training.[85] This technique enabled real-time 3D on-chip monitoring of locomotion patterns and neural activities of the *Caenorhabditis elegans* (*C. elegans*) at a 3D imaging rate of 100 Hz (Fig. 4b). In a DL-based lensless imaging system,[86] a forward model that incorporated light diffraction and spectral response of the optical elements in the system was employed to generate the training data. Apart from using simulated data, one could incorporate another imaging modality in the same system to generate training data *in situ*. This approach has recently been adopted in a microscope platform with both 3D light-field and 2D light-sheet imaging capabilities. By using the high-resolution and realistic ground-truth 2D images from the light-sheet microscopy for training, it can track the performance of the supervised CNN reconstruction of the raw light field microscopy (LFM) data during extended 3D time-lapse imaging.[87]

Instead of relying on the direct end-to-end models, there is an emergent class of physics-informed DL models that exploit the underlying physics of image formation to constrain the training process. Examples include specific transformation from raw measurements to 3D image,[91] or sparsity of the image.[92,93] DL with such "physics awareness" could overcome the common problem of tedious (or even unachievable) paired-image training. These models used untrained deep neural networks (DNNs) as prior models for image reconstruction, a concept called deep image prior.[94] For instance, a forward model of QPI formation (based upon light diffraction theory) is used to optimize the reconstruction without the need for traditional training followed by inference.[95] Another untrained generative DNN was used to synthesize Zernike polynomials combined with an ideal forward model, and was then trained to match the raw measurements of QPI. It was demonstrated to be effective in not only QPI reconstruction but also retrieval of aberrations.[40]

Incorporating the physics constraints has further shown promise in generalized learning in ill-posed problems, particularly for 3D QPI applications. For example, a similar concept of deep image prior has been applied to the 'missing-cone' problem in diffraction tomography (DT)[88] (Fig. 4c). Another example is to model the light propagation through heterogeneous samples as back-propagation in DNN. 3D RI tomogram can then be reconstructed using stochastic gradient descent in the highly scattering objects.[96] It can find applications in imaging organoid or organism on a microfluidic platform.

2.2.2 Super-resolution image reconstruction. Super-resolution microscopy (SRM) has revolutionized light microscopy by enabling superior image resolution using low-cost imaging optics[16] or unveiling nanometer-scale details inside the cells.[97–100] Over the past decade, various SRM methods have been adopted

Box 2 Common 3D imaging strategies

A series of imaging methods computationally reconstruct 3D images based on capturing a finite set of 2D images either along the axial dimension (or the through-focus direction), or from different illumination/detection angles (similar to X-ray tomography), without resorting to dense sampling of the entire imaged volume. These methods can be grouped into two categories. The first one takes the interferometric/holographic configurations, *e.g.* optical diffraction tomography (ODT),[67,68] and different variants of holographic lensless microscopy.[16,55] The second category takes the non-interferometric configurations, *e.g.* lens-based and lensless ptychographic microscopy,[69,70] light-field microscopy,[71,72] and incoherent lensless imaging using masks.[16] A strength in some of these methods is the ability to recover both the amplitude and quantitative phase information of the 3D samples – a method generically referred to as quantitative phase imaging (QPI).[73] QPI is proven to quantify important biophysical traits of cells and tissues, including dry-mass density and thus protein distribution without the need for labeling. This has also been used for label-free quantitative optofluidic imaging assays, *e.g.* QPI flow cytometry,[5,6,74] optofluidic ptychography,[75] and holographic lensless imaging assays.[55,76] 3D QPI (by the above-said methods) can further reveal 3D refractive index (RI) tomograms of the cells/tissues,[67,77–79] which is otherwise inaccessible by fluorescence imaging.

in different microfluidic and lab-on-a-chip imaging applications. Common strategies for SRM involve multiple incomplete image recordings in order to reconstruct the high resolution (HR) image. Examples include fusing multiple low-resolution (LR) images with sub-pixel shifts,[55,101,102] stitching multiple LR images in the Fourier domain (*e.g.* Fourier ptychographic microscopy[69,103,104] and SIM[22,102]), performing sub-pixel reconstruction in lensless ptychography[103,105] and combining a large number ($>10^3$) of LR frames to compute an HR image in SMLM.[106,107] However, the need for (repeated) multiple-image recording for HR reconstruction compromises imaging frame rate and further aggravates phototoxicity as well as photobleaching. DL strategies have thus been introduced to enhance the efficiency of the computational steps and to thereby speed up the temporal resolution with minimal phototoxicity (Fig. 4d).

In SMLM, LR images are sequentially captured by activating a tiny fraction of the well-separated single-molecule (fluorescence) emitters in a stochastic manner. With a sufficiently large number of LR frames, the emitter coordinates can be precisely localized by using different point spread function (PSF) fitting models (*e.g.* Gaussian,[108] double-helix,[109] and tetrapod[110]) and to yield an SR image. To increase the imaging throughput, one could activate the emitters at a higher density at the expense of computational cost. The resulting localization will also be affected as the emitters distributed in a 3D volume are densely packed or even overlapped in the 2D captured images. With sufficient simulated data,[111,112] or experimental data[12] for training, different DL-based SMLM methods (based on a variety of neural network architecture, *e.g.* CNN[111–114] and GAN[12]) outperform the standard fitting models in better localizing the emitter coordinates, extracting additional experiment-dependent parameters (*e.g.* aberration), and thus obtaining high-fidelity SR images, even for challenging cases with high-density emitters. Particularly, a GAN-based model with a sparsity constraint has demonstrated that SMLM images can be reconstructed from 100 times fewer LR frames than traditional methods, significantly improving temporal resolution and reducing phototoxicity/photobleaching effects.[12] Similar to 3D reconstruction, DL-based SR imaging reconstruction can be further optimized when multi-faceted priors are incorporated in the learning process (*e.g.* temporal stochasticity of emitters, photophysics of the emitters, PSF model and camera noise model). This concept has recently been proven effective in outperforming many existing DL and standard SR reconstruction methods in terms of accuracy and speed (Fig. 4e).[89] Further combined with hardware acceleration,[115] it might enable new capability of fast dynamic or high-throughput live-cell SMLM with reduced light exposure at ultra-high labeling density that could readily be integrated with the available microfluidic assays.[116–118]

Another class of DL strategies, generically called single-image SR (SISR), restores HR images directly from its LR counterparts and has also shown significant breakthroughs in SRM.[34,90,119,120] This approach is especially advantageous in high-throughput microfluidic applications as it requires no sophisticated imaging hardware or illumination strategies, and no extra compromise on imaging speed. DL-SISR methods typically require a sufficient amount of experimental or synthetic HR and LR image pairs for the training process, with a caveat that additional steps of image registration between HR and LR training pairs might be required.[34,119] This training strategy has been proven effective in yielding robust SISR image reconstruction using different deep neural network variants that are designed for faithful translation between HR and LR data.[34,121] Notably, the SISR reconstruction methods using GANs approach[90,119,122] can achieve superior SNR and imaging speed. They can also be applied in different imaging modalities like SIM, super-resolution radial fluctuations (SRRF),[123] and stimulated emission depletion microscopy (STED).[119]

2.3 Deep-learning image augmentation

Another exciting development in DL-based microscopy is to perform cross-modality inference (or augmentation) of image contrasts. This is an image-to-image translation operation by learning the image contrast information in one modality (*e.g.* fluorescence), which is often obscured or hidden in an image captured by another modality (*e.g.* bright-field, QPI and birefringence contrasts) (Fig. 5a). The predominant driver of this DL approach in microscopy is the quest for revealing the biochemically specific information of cells/tissues (*e.g.* localization of a certain type of proteins, morphology of a specific organelle within the cells) in the label-free images.[124,125] This capability has three-fold significance: (1) label-free imaging generally demands less complex imaging expertise and hardware, rendering this DL image augmentation approach favor for the cost-effective optofluidic imaging configuration; (2) fluorescent labels could result in different detrimental effects, such as compromising the cell viability,[126] disrupting cellular structures[127] and essential cellular functions.[128,129] Label-free imaging is thus suitable in visualizing living biological structures with minimal phototoxicity and no photobleaching. (3) This augmentation approach might help create a new knowledge base that correlates and transfers molecular specificity into the label-free morphological phenotypes of cells and tissue.

The available DL image augmentation methods share the common strategy that trains the DL models with the ground truth (fluorescence) images, captured by the same or a separate imaging modality, in order to learn the complex transformation from label-free to fluorescence images. Among the available neural network architectures, U-Net has been shown particularly promising as it can comprehensively capture image features at different spatial scales in hierarchy – favoring faithful image translation. Note that the U-Net can also be implemented in the GAN architecture for image augmentation.[130,131] Worth noting is its ability to handle both 2D and 3D images in predicting various cellular components, cell types and states.[124,125,132] Accurate

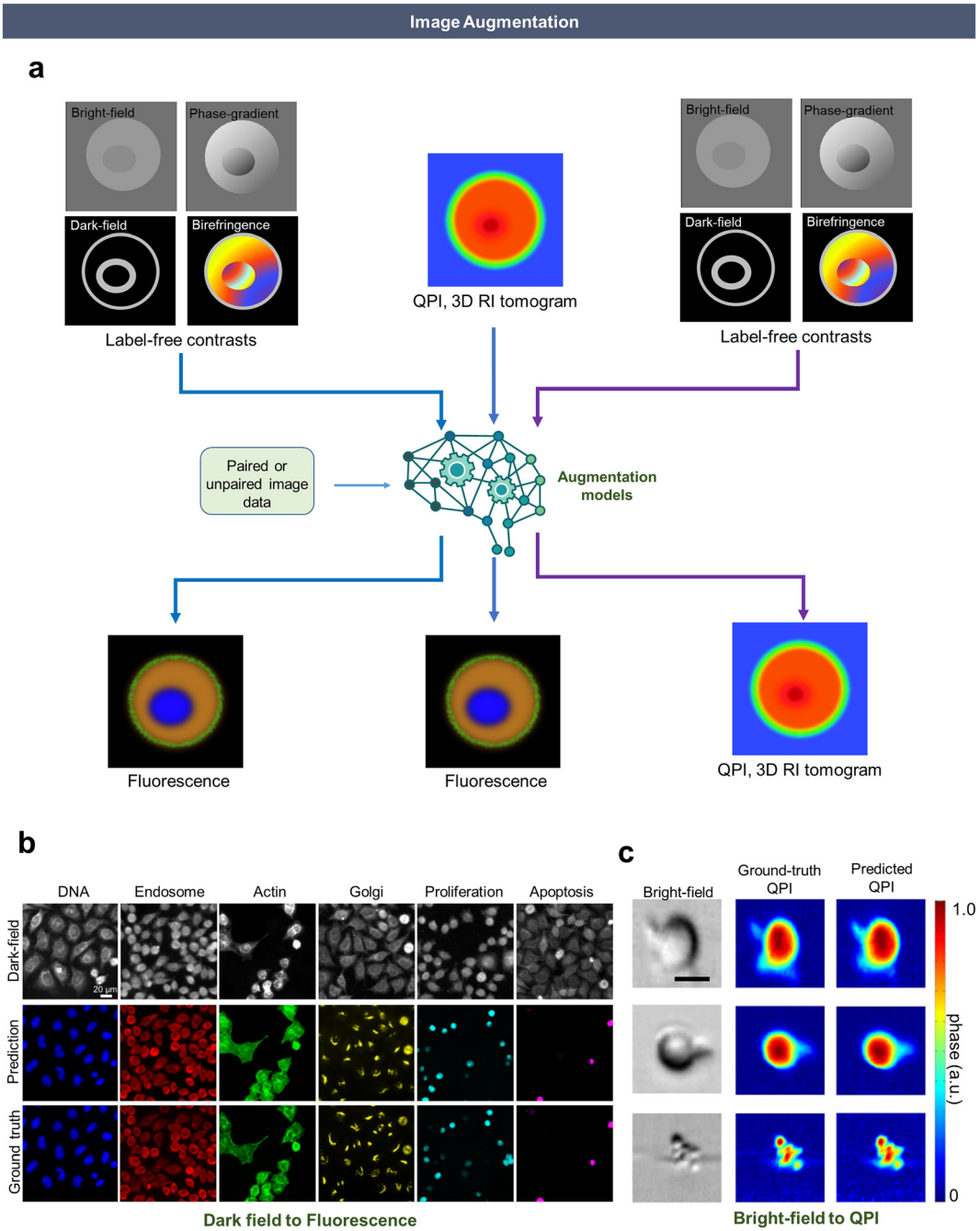

Fig. 5 (a) Common types of DL image augmentation: (left to right) label-free contrasts to fluorescence, QPI to fluorescence or label-free contrasts to QPI (b) prediction of six subcellular features including organelles and cell states from dark-field reflectance images of cells. Reproduced from ref. 132 with permission from CC BY-NC license. (c) An application of converting bright-field images to QP images using an autoencoder in a microfluidic imaging flow cytometry. Reproduced from ref. 130 with permission from AIP Publishing. Scale bars: (a) 20 μm, (c) 10 μm.

volumetric image augmentation can be achieved by a 3D U-Net at the expense of computational cost and time.[124] One can alternatively opt for a simpler U-Net design (*e.g.* 2.5D Net[133]) to reduce the computational complexity. To ensure no compromise in augmentation accuracy, it appears necessary to harness additional label-free contrasts for training, notably birefringence which reveals structural density and anisotropy.[133] The concept of the DL image augmentation can also be extended to many different types of contrast translation (Fig. 5b and c), such as bright-field to QPI,[130] QPI to fluorescence,[134,135] fluorescence to colorized bright-field (called digital staining).[131,136]

One key caveat of using adversarial models (such as GANs) for image augmentation is that they are susceptible to hallucination – a problem that the model tends to generate deceptive image patterns (to fool the discriminator) when there is insufficient training data. Another (common) issue is that the current trained inference models are likely not

suitable for generalizing to new samples/tests and inevitably require retraining. Different approaches could alleviate this problem, including unsupervised learning based on the cycle-consistent GAN (CycleGAN),[136] and incorporating the training data that contains minimally biased information (*e.g.* 3D RI tomogram[135]).

3. Optofluidics image analytics with deep learning

Image analytics covers a broad range of computational processes that convert images into desired readouts, such as detecting objects of interest (segmentation), performing quantitative analysis and prediction (classification and regression), and generating explanatory insights (image profiling) (Fig. 6, middle). All of these were conventionally done using expert-defined algorithms. However, they generally struggle to learn the highly complex and subtle information buried in the pool of image pixels. Using instead the DL models for image analytics has borne a lot of fruit, including the field of optofluidic imaging.

3.1 Segmentation

Prior to any meaningful biological image analysis, the objects of interest (*e.g.* cells, sub-cellular components, microbes colony, organisms) should be distinguished from the irrelevant background – a critical step called semantic segmentation. In many optofluidic imaging applications, further instance segmentation is needed for operations such as detection,[137] tracking[138] and quantification.[139–142] To support in-depth morphological analysis,[143] further precise outlining of the cell shape is a requisite. The performance of segmentation is highly influenced by the type of image contrasts (*e.g.* label-free *versus* fluorescence), spatial complexity of the samples (*e.g.* tightly packed and overlapping cells) and image fidelity (*e.g.* non-uniform background intensity[139]). Traditionally, a wide range of algorithms such as thresholding, edge detection, watershed, can segment batches of images semi-automatically. However, manual tuning of parameters according to the image conditions (*e.g.* image intensity, image quality, cell density *etc.*) is often needed in these algorithms. To this end, DL-models have been developed to achieve automated segmentation with better accuracy and generalization (Fig. 7).

Identifying the cell bodies and nuclei in microscopy is very often the initial task required in many quantitative biological analyses. Significant effort has been made in DL nuclei segmentation in fluorescence microscopy.[144–146] A worldwide competition with 3891 teams[144] showed that CNN models (*e.g.* U-Net, Mask R-CNN, feature pyramid network (FPN)) generally outperform the classical segmentation. Furthermore, they has brought fruition to optofluidic imaging, including segmentation of bacteria in the microfluidic 'mother machine',[147] monitoring of microstructure-trapped yeast cell divisions,[148] tracking the lineage of *E. coli*,[149] analysis of biofilm,[150] and on-chip morphological analysis of oocytes,[151] and sickle red blood cells.[143]

Among all CNN models, U-Net[35,152] has inspired several powerful segmentation pipelines, *e.g.* DeLTA,[138,149,153] Stardist,[154] Cellpose[150] to name a few. Many CNN-based pipelines generally aim to solve the boundary detection problem that involves pixel-wise classification of the background, the interior region and the boundary of the cell

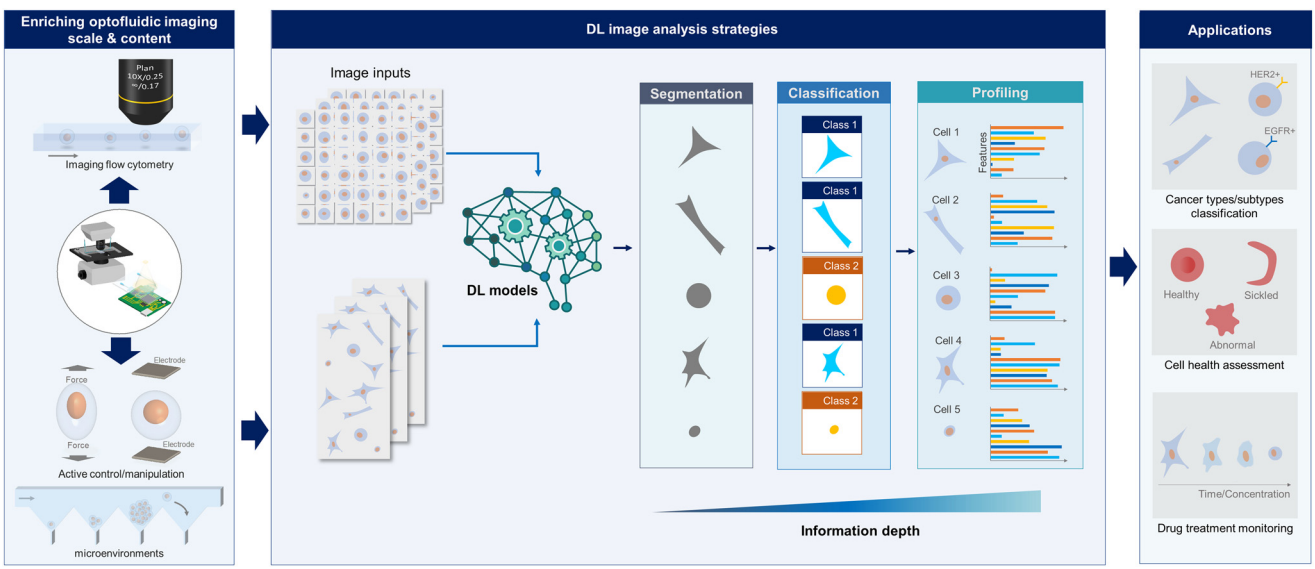

Fig. 6 DL image analysis strategies. Image read-outs generated from microfluidic chip platforms (*e.g.* microfluidic imaging cytometry, impedance cytometry, deformability cytometry, controlled microenvironments) are fed into the DL models for different common types of image analytic tasks: image segmentation, image classification and profiling. The applications cover from cancer subtyping, cell health assessment to drug screening assays.

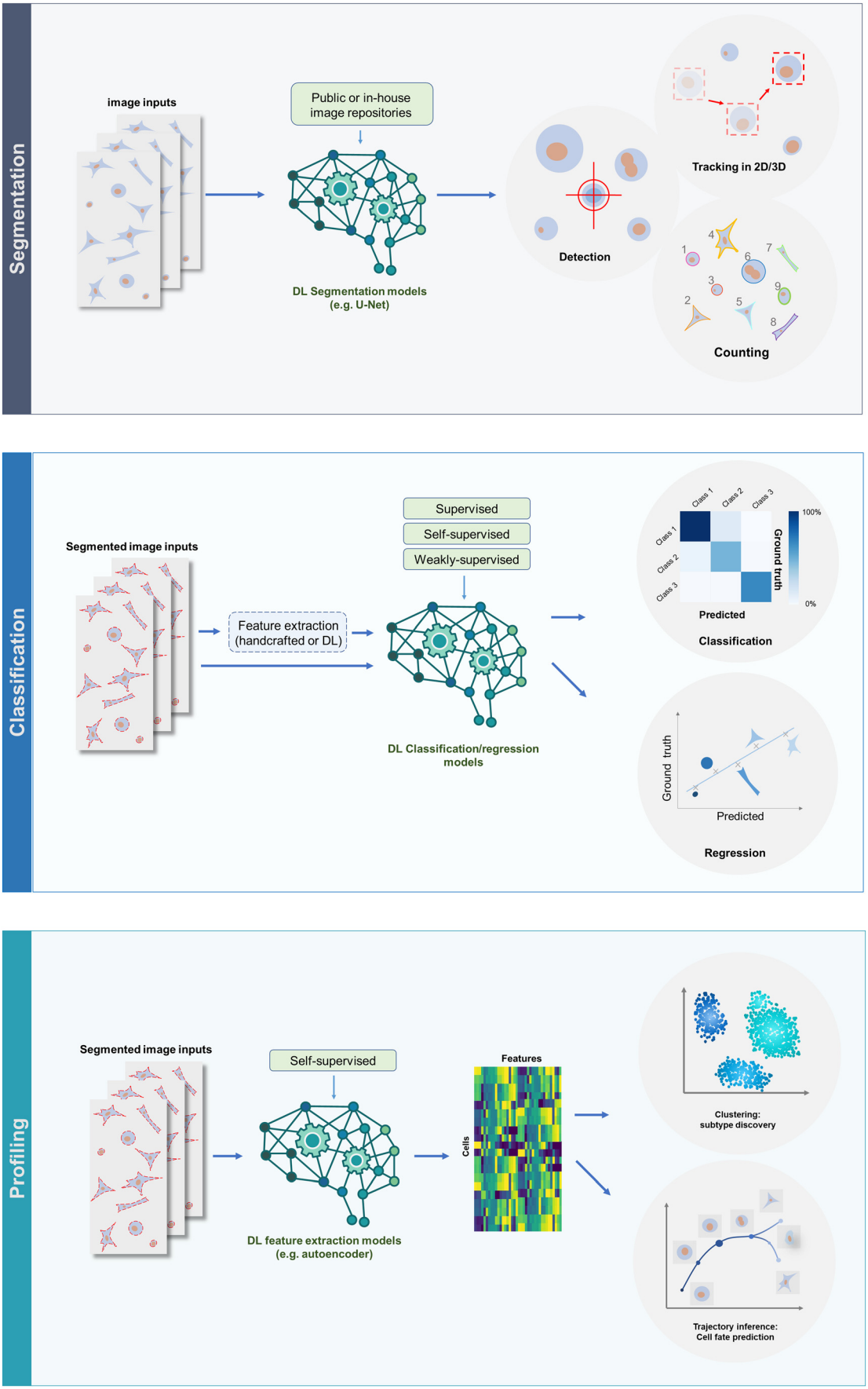

Fig. 7 Key strategies of optofluidic image analytics with deep learning: (top) image segmentation, (middle) image classification/regression, and (bottom) image-based profiling.

(or nucleus). The key differences among them often lie in the additional processing steps that define the novel metrics used for classifying the segmented regions (*e.g.* defining the spatial gradient topology in Cellpose, and setting the star-convex polygons in Stardist), as well as the data training strategy (*e.g.* data augmentation in nucleAIzer[146] for better generalization).

The state-of-the-art DL segmentation pipelines are now increasingly generalizable to different imaging modalities and conditions, diverse data types (*i.e.* different cell types and image contrasts[152,153]), and even extendable to 3D imaging scenarios (*e.g.* 3D cell cultures, organoids, and small animals). Nevertheless, these pre-trained models should always be adopted with caution, especially on new unseen data. In many cases, it is essential to have the option to re-train models (with optional transfer learning) using additional annotated data of interest in order to produce reliable results. Thanks to the tremendous progress made in the community, there are a growing number of public cell image repositories, each of them containing thousands to millions of cell images with different image contrasts (*e.g.* fluorescence image datasets from EVICAN,[155] Human Protein Atlas,[156] Broad Bioimage Benchmark Collection,[157] and 2018 Kaggle Data Science Bowl;[158] the recent label-free phase-contrast image datasets from LIVECell[159]), for continuing training purpose. Multiple open-source software packages are now available for users with or without DL expertise to conduct DL microscopy image segmentation and downstream analytics. As far as the generalizability concern, some of them allow the users to have flexible options of retraining in a single workflow for streamlined model training (*e.g.* Ilastik,[160] ZeroCostDL4Mic[161]).

A caveat of extending the existing 2D DL models for 3D image segmentation is the anisotropic 3D spatial resolution present in many 3D imaging modalities. Proper modifications of the CNN architectures or the pipeline steps are usually needed, *e.g.* including additional convolution and pooling layers for the dimension with the poorest resolution (U-Net),[152] using ensemble of models that used various number of image stacks as input (Cdeep3M)[162] and 2D slicing of the volume along all 3 dimensions as model inputs (Cellpose).[153]

It is worth mentioning that accurate segmentation facilitates the tracking of cell and cell nuclei in live-cell imaging applications, including monitoring signaling dynamics, detecting mitosis,[163] and cell motility,[164] many of which can be conducted in the lab-on-a-chip platforms. An open-source package, TrackMate 7, has recently been released with a user-friendly application programming interface (API) that integrates many of the aforementioned state-of-the-art segmentation algorithms into tracking pipelines.[165] This type of integrated pipeline can democratize DL image segmentation methods for resolving diverse tracking problems, and accelerating biological discovery.

3.2 Image classification

Image classification aims to assign a meaningful label to an image or the object(s) in the image – one of the most prominent successes of DL computer vision. As advanced microscopy continues to scale up the spatiotemporal resolution, throughput, and choices of imaging contrasts, optofluidic imaging is anticipated to further push the frontier of DL image classification in screening and diagnostic applications. Particularly, it becomes increasingly practical for harnessing the cell morphology read-outs to identify genetic & chemical perturbations,[166,167] predict metastatic potentials,[168] and many more.

The input of DL image classification can be the raw or processed 2D/3D image itself, the handcrafted image features (*e.g.* pixel intensities, textures, size, shape, *etc.*[169]), or the latent features extracted by the DL models through self-supervised learning (*e.g.* autoencoder[170–172]) (Fig. 7). The advantage of defining morphological features for image classification (either based on the handcrafted or deep-learnt features) is that it allows us to establish the morphological "fingerprint" (profile) that can underpin the biologically relevant conditions (discussed in section 3.3) Image classification results based on handcrafted features traditionally offers better biological interpretability. In contrast, the result using the latent features self-learnt by DL or directly using the image as input often struggles to explain how the "black-box" DL models learn the biologically meaningful information from the image, even though the classification accuracy ended up superior to the case using handcrafted features. While there is still no consensus on the best solution for gaining the interpretability from DL models, different strategies have already shown convincing progress, *e.g.* investigating the activation maps of the intermediate layers of the neural network for gaining more insight into where the network focused on,[143,173,174] correlating the latent features with the known handcrafted features.[170,172]

Depending on the availability of training data, one can choose different learning models for classification: supervised learning from the well-annotated data or weakly-supervised learning using the inexact but relevant labels as ground truth.[175] It is not always feasible or practical to generate a large-scale annotated database for training the supervised model, *e.g.* high-throughput imaging cytometry where thousands to millions of cells per class. To address this issue, a weakly supervised model is an economical alternative in which a model can be trained using annotated data that do not exactly describe the targeted classes, but the experimental setting of the images. For instance, one can learn the generic features that represent cells based on common metadata (*e.g.* dates of experiments[176]) and use them for the main classification task.

3.3 In-depth analysis: image profiling and beyond

In order to apprehend which aspects of the cell/tissue morphology give rise to the image classification results, one should go beyond the image classification labels generated by the DL models and analyze the handcrafted image features or the latent features extracted by the DL models

(through self-supervised learning).[170] This approach allows us to identify the morphological "fingerprint" (profile) that underpins the biologically relevant conditions. It is essentially similar to the common omics strategies, *e.g.* gene expression and protein profiles for transcriptomic and proteomics study, respectively. These image-based profiling strategies are proven promising in mining specific patterns in the profile to reveal disease-associated phenotypes,[168,177,178] predict cell health[179] and toxicity[15,180] or mechanism of action of drugs.[167,181]

Empowered by the massive data size obtained from microfluidic platform,[3] the image profiles in high-dimensional algorithms enable high-throughput and high-content analysis to uncover hidden subpopulations[182] and trajectories of cell progression/development.[175,183] (Fig. 7) Its compatibility with live-cell imaging enables correlation studies with other downstream analyses (*e.g.* transcriptomic)[168] for gaining deeper biological insights. More importantly, image-based profiling can capture biological information obscured in transcriptional profiling.[184] Combined with the advanced genetic manipulation toolboxes (*e.g.* RNA interference (RNAi), or CRISPR), which are now compatible with the microfluidic designs,[185–187] image-based profiling thus offers an attractive solution for mapping the genetic perturbations to changes in the morphological phenotypes and thus cell functions/states.[188–190] For instance, early attempts using RNAi screen have already been taken to identify genes that influence the mechanical property of cells probed in the microfluidic cell deformability imaging assays.[191]

There is a caveat to practicing image-based profiling. While more biological information is likely encoded with a more extensive (*i.e.* higher-dimensional) profile, it is also more challenging to tease out the relevant and reproducible information from imaging noise, technical experimental variations/biases and other unrelated signals, *i.e.* curse of dimensionality. Different levels of DL supervision, based on either handcrafted or self-learnt latent features, could be adopted to augment the discriminative power of the DL models. For instance, in supervised learning, classical feature ranking and selection can identify the image features that are more susceptible to the out-of-focus imaging conditions, *e.g.* in imaging flow cytometry.[74] In self-supervised learning, a DL model, *e.g.* autoencoder, can be used to extract the set of latent features that are most representative of the target cells and their morphological changes based on their cell types,[171] and states.[170,172] Recently, weakly-supervised learning allowed one to annotate the image label that is not directly relevant to the cell morphology but is a more easily obtainable label (*e.g.* multiple replicates of the experiments on different dates). This method could leverage the seemingly redundant information to distil a robust profile.[192]

3.4 DL analytics strengthened by microfluidics

While DL revolutionized image analytics, microfluidics further substantiated the power of DL image analytics in unique ways to spearhead more applications.

3.4.1 Scaling up throughput by imaging flow cytometry (IFC). The advances in microfluidic particle-focusing[193–196] have enabled in-focus single-cell imaging even under high-speed microfluidic flow. This capability has unleashed a rich collection of high-throughput microfluidic IFC platforms that can efficiently generate a massive amount of high-quality images of single-cells at the scale of 100 000's of cell images per experiment, even reaching >1 000 000 in some cases.[6] The availability of such large and heterogeneous image datasets is advantageous for training potentially generalizable DL models for complex image classification tasks as the common data augmentation such as image flipping, rotation, and scaling is no longer needed.

Leveraging this large-scale capability, many microfluidic IFC modalities have demonstrated impressive DL image classification beyond using standard fluorescence imaging, but also a wide variety of label-free imaging approaches, such as brightfield,[171] quantitative phase,[5,197] Raman,[176,198] or a combination of them.[198] They have opened new possibilities in many once-inconceivable label-free IFC applications, including classification of cancer (sub) types[6,199,200] and stages,[174] blood cell health assessment,[171,175,201] drug treatment monitoring,[202,203] detection of rare cancer cells in blood[6,176,204] (Fig. 6, right).

3.4.2 Diversifying image read-outs by microfluidics. Thanks to its design flexibility at the microscale, microfluidic platforms allow additional precise control and manipulation of the imaged samples (*e.g.* force, microenvironment (Fig. 6, left)) that are absent or challenging in the imaging assay based on the standard microscope settings. This is particularly advantageous for probing complex spatiotemporal characteristics of the biological samples, and thus a more extensive set of image read-outs – enriching the information content for DL image analytics. For example, optofluidic imaging has been employed to effectively probe the mechanical properties of cells,[143,205–207] which are proven biomarkers for different disease conditions such as cancer metastasis, inflammation and cardiovascular diseases.[208,209] Other active microfluidic designs are expected to be increasingly compatible with optofluidic imaging, such as on-chip impedance measurements of microparticles and cells.[210,211]

Furthermore, microfluidics can now be designed to mimic *in vivo* microenvironments for organoids and tumorspheres. These chips helped in developing AI classification models for classifying adhered cancer cells,[212] drug response monitoring,[213,214] predicting tumorsphere formation[215,216] and determining metastatic potential.[217] Additionally, creative microfluidic chip designs had been exploited to enable high-throughput imaging in an arrayed format.[218,219] These methods could hold great promises for in-depth image analytics not only because of their large-scale operation, but also the richer image read-outs corresponding to diverse sample conditions precisely controlled in the microfluidic environment.

4. Intelligent image-guided autonomous microfluidics

Beyond advancing image computation and analytics,[220,221] the bigger impact of adopting DL in optofluidic imaging is arguably in enabling self-driving microfluidics. The concept is to harness the deep learnt information as an adaptive feedback control that interacts with the optofluidic imaging platform. Analogous to autonomous vehicles,[222] the outputs of the DL models used in the imaging system (*e.g.* detected cells/tissue regions and their specific spatiotemporal behaviors) can guide the system itself (1) to continuously optimize the imaging performance and (2) to control/coordinate the process of the entire microfluidic experiments/assays all in real-time.

4.1 "Smart" optofluidic imaging

Closed loop feedback for optimizing the imaging quality in a microscope has long been practiced, such as auto-focusing and aberration correction by adaptive optics.[223] One notable example is the Autopilot framework for adaptive imaging operation, which could readily be applied to optofluidic imaging.[224] Further leveraging the increasing context-awareness of the DL algorithms (*e.g.* image restoration by CARE[34]), one can create "smarter" autopilot solutions that recognize the more complex imaging scenarios and thus automatically reconfigure the microscope to obtain the best imaging quality and consistency (Fig. 8). For instance, the system can be trained to determine which events to image. This is pertinent to on-demand time-lapse image capture for long-term monitoring experiments, *e.g.* the development of zebrafish, fruit fly and mouse embryos. Also, the DL tasks of segmentation, profiling and other deep analytics can also actively guide the system on how specifically to image the sample in the best optimal and efficient manner. It can involve active on-demand control of the imaging positions, sample orientation (in 3D),[225] as well as adaptive adjustment of illumination and speed settings for augmenting imaging SNR.[226,227] More complex controls are possible, such as real-time correction for optical aberration, and sample motion artefacts. The key challenge is to minimize the DL inference latency (or time delay) introduced by the computational hardware (as discussed in 4.3) in order to ensure a timely response of the feedback.

4.2 Autonomous microfluidics control

The smart feedback control can further be exploited to automate a wide variety of real-time microfluidic operations (*e.g.* microfluidic heat/mass transport control and microparticle manipulation), and thus support autonomous lab-on-a-chip assays. This closed-loop synergism of microfluidics and DL is on the horizon and begins to impact the advance in chemical sciences and biological/biomedical research. For instance, by visualizing the microfluidic flow rate in real-time, an optofluidic imaging system can be trained through reinforcement learning to control the size of the water-in-oil droplets generated on-chip.[228] As the integrated DL optofluidic imaging platforms become increasingly promising in automating microparticle encapsulation,[229] controlling droplet formation stability, and even evaluating chemical composition in droplets,[230] we anticipate that these integrations could accelerate the widespread utility of "intelligent" microfluidic technologies in chemical reaction optimization,[231] as well as microparticle synthesis and optimization.[232,233]

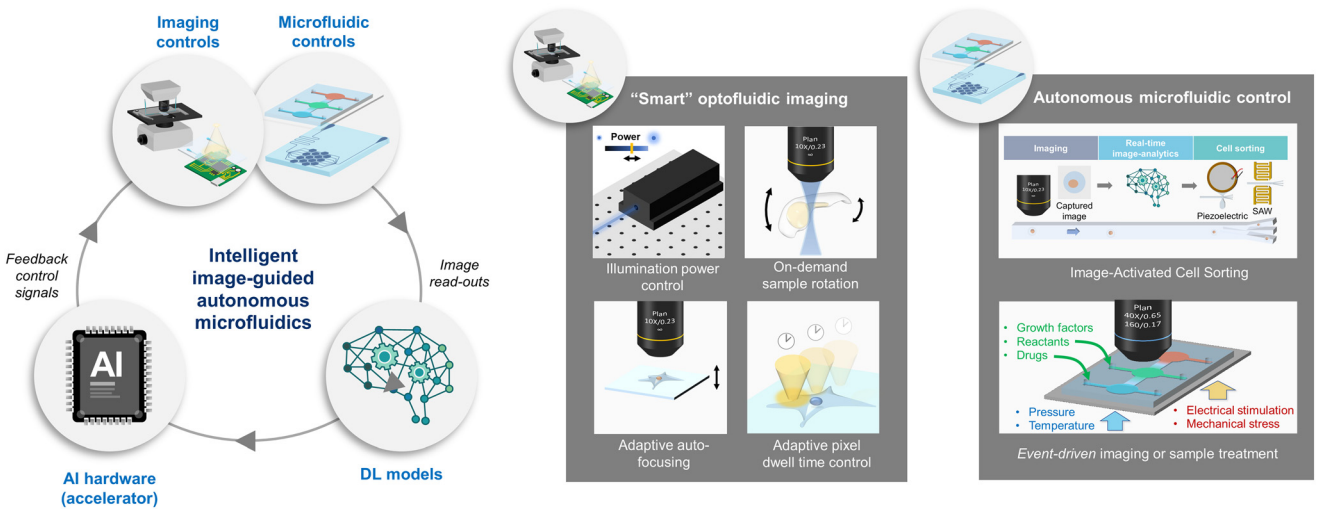

Fig. 8 Generic strategies of intelligent image-guided autonomous microfluidics: (1) DL-driven imaging feedback control for "smart" optofluidic imaging (*e.g.* adaptive illumination power control, on-demand sample rotation, adaptive auto-focusing, and pixel dwell time control), and (2) DL-driven autonomous microfluidic control (*e.g.* image-activated cell sorting, and event-driven imaging or sample treatment in the lab-on-a-chip platforms, especially organ-on-a-chip).

Another notable example is image-activated cell sorting (IACS).[229,234–237] In its generic form, IACS first captures images of single cells, followed by real-time cell morphology analysis in order to determine which cells should be sorted by the microfluidic sorter, which can commonly be actuated by the surface acoustic wave (SAW),[237] or piezoelectric transducers[234] (Fig. 8). The sorted cells are typically sent to downstream molecular analysis, *e.g.* bulk or single-cell sequencing. In contrast to the standard fluorescence-activated cell sorter (FACS) which is blind to the spatial information of cells (*e.g.* organelle morphology, intracellular protein localization), IACS enables deeper investigation of complex (biophysical and/or biochemical) morphological phenotypes of cells at high throughput read out by different image contrasts, *e.g.* fluorescence,[234,235] bright-field,[237] Raman.[17] Particularly powerful is the combination of IACS with the burgeoning single-cell multi-omics technologies. Such integration could redefine our understanding of how the molecular signatures and pathways in the cells may drive a specific form of cell morphology. This could incentivize new streamlined strategies for cell-based assays that could directly impact diverse areas of applications, including cell atlas research, drug discovery, and cell therapy applications.

Available IACS systems mainly rely on two approaches for triggering the sorting action: (1) using the common classifiers, *e.g.* decision trees,[235] support vector machine,[238] based on the morphological features (10's – 100's) extracted from the images, including cell size, shape, and textures; (2) using deep neural network architectures (*e.g.* multilayer perceptrons (MLPs)[237] or CNN[239]) to classify the targeted cell population to be sorted. The main caveat is that the computation speed for making classification decision has to be meticulously synchronized with the upstream imaging speed and the downstream cell sorting speed. This is particularly challenging for large-scale screening applications which require a high sorting speed beyond 100 to even 1000 cells per s, as discussed in the next section.

Autonomous microfluidics could perform even more sophisticated tasks in which multiple on-chip controls can be triggered by DL in a concerted manner. Initial success has been demonstrated in an automated microfluidic reactor.[232] Guided by the neural-network-assisted (infrared) image analysis, microfluidic catalytic reactions can be optimized in real-time, and in a much faster manner compared to the standard methods (reduced from weeks to hours). As tools and methods for automated microscopy become increasingly accessible, similar strategies of image-guided autonomous microfluidics are likely to impact a broader scope of applications. Examples include the open-sourced tool NanoJ-Fluidics,[240] which is an automated syringe pump array that can exchange fluids to perform fixation and labelling at the imaged sample, and thus supports automate complex imaging protocols. It was demonstrated to perform cell fixation triggered when mitotic events were captured by the microscopy – allowing *in situ* correlative live-to-fixed SMLM.[240]

It is anticipated that further incorporation of DL-assisted triggers could make automated image-based assay more intelligent, *i.e.* capable of supporting event-driven imaging or sample treatment and facilitating highly flexible optofluidic imaging workflows and microfluidics exchange. This capability is particularly beneficial to organs- or organoids-on-chips,[241,242] which are largely built upon microfluidic platforms for probing and evaluating complex physiological responses of the organs/organoids in an *in vitro* manner. These systems have shown many promising applications ranging from disease modeling[243] to drug screening.[244,245] To ensure proper organogenesis on-chip, the biochemical and biophysical conditions have to be precisely controlled during the course of experiment. Autonomous microfluidics in this case can use DL to analyze the image data, together with the data collected by other sensors integrated in the same system,[246] in order to optimize the culture conditions (*e.g.* reactants, temperature, and pressure in the microreactors) and automation of biochemical/physical stimuli (*e.g.* growth factors, drugs, electrical stimulation, mechanical stress) (Fig. 8). While it is currently still a nascent field, initial success, *e.g.* DL-guided bioreactor control,[247] has shown the encouraging potential in scaling up these autonomous organoids-on-chips for accelerating high-throughput screening of drug compounds in physiologically relevant models – ultimately facilitating timely prediction of tumor response to chemotherapy.[248]

4.3 Hardware challenges

It becomes clear now that the extraordinary algorithmic development of DL has outpaced the progress in the advanced hardware for processing the algorithms. Since 2012, the computational load of DL has generally doubled every 3.4 months and has grown by >300 000 times compared to the pre-2012 era.[249] To fill this gap, there is a pressing need for hardware accelerator innovations that supports real-time DL operations as in autonomous microfluidics. Currently, large-scale DL computation can be accelerated by graphic processing unit (GPU), application specific integrated circuit (ASIC) (*e.g.* tensor processing unit (TPU)[250]), and field-programmable gate array (FPGA).[251] While many computationally intensive DL models can be trained on either local GPUs or in data centers, these solutions are costly and not always compatible with lab-on-a-chip applications, especially those mandate low-latency (*i.e.* fast inference) image-guided feedback and thus control.

To this end, FPGA appears to be an attractive solution for accelerating DL inference tasks as it is a reconfigurable hardware that implements only the necessary hardware logic according to the target algorithm, and thus obviates the hardware redundancy. Hence, compared with CPU and GPU platforms, FPGA enables highly efficient high-throughput computation and thus favors real-time DL image-based inference and multiplexed feedback control, as in IACS and organoid-on-chip applications. In these applications,

inference latency should ideally be minimized to support real-time autonomous operation. Inference acceleration is thus the key specification to be optimized through meticulous co-design of FPGA hardware and DL algorithm.[251] In many organoid-on-chip applications in which the inference latency of seconds is sufficient for generally on-chip feedback control (*e.g.* regulating microreactor's conditions, triggering biochemical/biophysical stimulations), and can be readily supported by many off-the-shelf FPGA platforms. The key challenge lies in coordinating the precise latencies of multiple DL-triggered controls to the chip. On the other hand, the inference latency of IACS is needed to be much shorter, on the order of milliseconds or less, in order to ensure high-throughput cell sorting. This is a challenging task as all the computation steps of image acquisition, processing (including basic filtering and segmentation, *etc.*)

Table 1 Summary of major DL training strategies adopted in optofluidic imaging

Operations	Major training strategies	Strengths and potentials	Caveats	Ref.
Image formation				
Image restoration	Supervised	- Straightforward operation to restore image quality	- Paired image training datasets are required	23, 31–34, 41, 46, 47, 49
	Self-supervised	- No paired image training datasets are required	- The modality-specific assumptions of the image characteristics	36–39, 42, 43
	Deep prior	- Complete model retraining is not required	- Expertise knowledge in modality-specific imaging physics is required	40, 45, 50–52
3D image reconstruction	Supervised (by simulated training data)	- No excessive experimental image or additional 3D imaging modality for training	- Expertise knowledge in modality-specific imaging physics is required	84–86
	Supervised (by another 3D imaging modality)	- Realistic and high-quality datasets for training	- An additional 3D imaging modality is required	87
	Deep prior	- No additional 3D imaging modality is required for training - Generalized learning of ill-posed problems (*e.g.* 'missing-cone' in diffraction tomography)	- Expertise knowledge in modality-specific imaging physics is required	88, 94–96
Image super-resolution	Supervised (by simulated or experimental LR data)	- High-fidelity SR image reconstruction can be achieved	- Sufficient paired training datasets are required	12, 34, 90, 111–114, 119–123
	Deep prior	- Both the reconstruction accuracy and speed can be improved	- Expertise knowledge in super-resolution imaging physics is required	89, 115–118
Image augmentation	Supervised	- Demand for expert knowledge in complex imaging hardware can be relaxed - Fluorescence labelling that compromises live cell imaging can be bypassed - New knowledge base that correlates different image contrasts can be generated	- Generalizability to different sample types and imaging scenarios is challenging - DL models are likely susceptible to the hallucination problem	124, 125, 130–136
Image analytics				
Segmentation	Supervised	- Current methods are broadly generalizable	- Many methods require labor-intensive annotation	138, 143–154, 160–165
Classification	Supervised based on handcrafted features or self-supervised by DL latent features	- Favorable for downstream morphological profiling - Handcrafted features allow better interpretability	- DL latent features generally lack the ability to offer biologically meaningful information from the image	143, 169–172, 205, 207, 212, 217
	Supervised (based on their image input directly)	- Simple, plug-and-play, real-time operation is allowed	- The "black box" lacks the interpretability of the classification results	5, 6, 174, 197–204, 206, 211–216, 218
	Weakly-supervised	- Strict dataset annotation is not mandated	- Extra datasets from separate tests/batches are required for "weak" supervision	175, 176
Profiling	Self-supervised	- No biased handcrafted feature selection is needed	- DL latent features generally lack the ability to offer biologically meaningful information from the image	15, 167, 168, 170–172, 177–181, 184–190, 205, 212
	Weakly-supervised	- Strict dataset annotation is not mandated	- Extra datasets from separate tests/batches are required for "weak" supervision	192

and DL inferences have to be completed within such a short time delay, not to mention that this delay has also to be adjusted to ensure the sorting event precisely coincided with the arrival time of the moving cell at the sorting region in the microfluidic channel.

A complete DL inference implementation on FPGA remains a daunting task. This is mainly because of their limited chip memory and low aggregate bandwidth (compared to GPUs) for handing large-scale DL models. To this end, current strategies for practical IACS are generally bound by the trade-off between the overall hardware and software complexity. In a notable IACS demonstration, a heterogeneous system comprising CPUs, GPUs, and FPGAs connected on an all-IP network was proven feasible to achieve an overall latency of ~30 ms by offloading most of the DL image analytics (including an eight-layer deep CNN) to the GPUs whereas the FPGA was mainly used for predicting the latency at the sorter.[252] Further refinement of the hardware has shown to achieve the IACS throughput of ~2000 events per second.[234] The latency can be greatly shortened by reducing the complexity of the DL analytics. In the IACS approaches with the inference latency of 1 ms, the analytics pipelines commonly include initial feature extractions from the images followed by classical ML classifiers,[238] or MLP,[237] without employing the CNN models. In these demonstrations, the full benefit of FPGA in reconfigurability and latency has not been exploited in optofluidic imaging until recently. A deeply pipelined FPGA design has shown that CNN inference can be implemented in parallel to the series of cell image processing steps at high throughput.[253] This *in situ* operation, which favours ultrashort inference latency, is made possible by quantizing the CNN network parameters in lower-bit precision representations (*e.g.* 8-bit). The rationale is to balance the computation and memory load on FPGA without significantly sacrificing the DL model accuracy.[254,255] Such strategy has been demonstrated in a label-free classification of peripheral blood mononuclear cell (PBMC) subtypes with an ultralow classification latency of 34.2 μs with over 95% end-to-end accuracy and at an imaging throughput >29 000 cells per s.[253] This might be a potentially practical solution for further scaling up the throughput of future IACS applications.

5. Concluding remarks

Moving forward, the development of DL optofluidic imaging in the three aspects discussed in this article (summarized in Table 1) is poised to be increasingly diversified, involving a wide-ranging mix of disciplines, *i.e.* microfluidics, imaging instrumentation, DL algorithms and DL hardware accelerator. Each of them entails specialized technical expertise, which is not always easily transferrable between disciplines. Hence, successful deployment of DL optofluidic imaging requires special attentions in the following areas that could drive innovations at this multidisciplinary intersection.

First, it is critical to ensure easy (and open) accessibility to DL tools as well as relevant image data repositories. It helps accelerate the dissemination and interoperability of the DL methods (from model to and validations) in optofluidic imaging. Many DL imaging processing and analytics tools are now made easily accessible to researchers, without requiring expert programming skills. Apart from that the major microscope manufacturers have launched their image analysis software that include DL functionalities (*e.g.* Denoise.ai by Nikon, Apeer by Zeiss and Aivia by Leica), there are a number of open-source and free platforms. For instance, an open cloud-based resource (on Google Colab), called ZeroCostDL4Mic,[161] is available for free, and powerful DL image restoration and reconstruction. Another open-source platform, ImJoy[256] offers an easy-to-use user web-based interface.

Second, curated repositories of high-quality image data have to be standardized and widely accessible to the optofluidic imaging community in order to facilitate large-scale DL model training, allow systematic data integration, improve model scalability, interoperability and thus generalizability for future exploration. Taking cell image datasets as an example, there are many publicly available repositories established by research institutions[257,258] and the biotechnology industry.[259] For example, the Image Data Resource (IDR) catalogues a wide range of cellular image datasets recorded under different experimental conditions (*e.g.* genetic mutants and drug compounds).[260] The optofluidic imaging community is encouraged to take the coordinated initiatives for contributing to these existing data repositories or establishing an optofluidic-oriented one, as long as these efforts favour compatible data sharing/reuse and thus accelerate DL development and optimization for the optofluidic imaging applications.

Lastly, the optofluidic imaging community should also leverage the parallel advancement in DL hardware accelerator, which might provide a new thrust in the next-generation autonomous lab-on-a-chip. In order to realize seamless integration of microfluidics and DL hardware, it is necessary to call for deeper and close-loop collaboration among experts in DL hardware, imaging, and DL algorithms to come up with the optimal solutions tailored for different lab-on-a-chip platforms. Beyond the aforementioned solutions based on GPUs and/or FPGAs, the emerging DL accelerators, notably neuromorphic computing,[261] which has shown appealing performance in edge processing for point-of-care and wearable biosensors. These novel devices share a lot of common design specifications with microfluidic platforms, including real-time inference, online learning, and low-power consumption. In closing, the merging of DL and optofluidic imaging has created a whole new landscape in lab-on-a-chip, stretching far beyond the *status quo*. Collective efforts are underway to overcome the challenges mentioned above. It will not be surprising to anticipate in the coming years that many emergent strategies of DL optofluidic imaging integration could be turned into indispensable

toolboxes that advance research in chemical and biological sciences, and even in clinical diagnostics, prognostics, and therapeutics.

Conflicts of interest

J. W. is a shareholder of Conzeb Limited, which provides no funding support to this work.

Acknowledgements

The work is supported by the Research Grants Council of the Hong Kong Special Administrative Region of China (grant no. 17125121, 17208918, RFS2021-7S06, C7047-16G), Platform Technology Funding of the University of Hong Kong.

References

1 A. Manz, N. Graber and H. M. Widmer, *Sens. Actuators, B*, 1990, **1**, 244–248.
2 L. Xin, W. Xiao, L. Che, J. Liu, L. Miccio, V. Bianco, P. Memmolo, P. Ferraro, X. Li and F. Pan, *ACS Omega*, 2021, **6**, 31046–31057.
3 H. Kobayashi, C. Lei, Y. Wu, C. J. Huang, A. Yasumoto, M. Jona, W. Li, Y. Wu, Y. Yalikun, Y. Jiang, B. Guo, C. W. Sun, Y. Tanaka, M. Yamada, Y. Yatomi and K. Goda, *Lab Chip*, 2019, **19**, 2688–2698.
4 T. T. Wong, A. K. Lau, K. K. Ho, M. Y. Tang, J. D. Robles, X. Wei, A. Chan, A. H. Tang, E. Y. Lam and K. K. Wong, *Sci. Rep.*, 2014, **4**, 1–9.
5 K. C. Lee, A. K. Lau, A. H. Tang, M. Wang, A. T. Mok, B. M. Chung, W. Yan, H. C. Shum, K. S. Cheah and G. C. Chan, *J. Biophotonics*, 2019, **12**, e201800479.
6 D. M. D. Siu, K. C. M. Lee, M. C. K. Lo, S. V. Stassen, M. Wang, I. Z. Q. Zhang, H. K. H. So, G. C. F. Chan, K. S. E. Cheah, K. K. Y. Wong, M. K. Y. Hsin, J. C. M. Ho and K. K. Tsia, *Lab Chip*, 2020, **20**, 3696–3708.
7 K. AbuZineh, L. I. Joudeh, B. Al Alwan, S. M. Hamdan, J. S. Merzaban and S. Habuchi, *Sci. Adv.*, 2018, **4**, eaat5304.
8 T. J. Levario, B. Lim, S. Y. Shvartsman and H. Lu, *Annu. Rev. Biomed. Eng.*, 2016, **18**, 285–309.
9 Y. LeCun, Y. Bengio and G. Hinton, *Nature*, 2015, **521**, 436–444.
10 A. Krizhevsky, I. Sutskever and G. E. Hinton, *Advances in neural information processing systems*, 2012, vol. 25.
11 C. Belthangady and L. A. Royer, *Nat. Methods*, 2019, **16**, 1215–1225.
12 W. Ouyang, A. Aristov, M. Lelek, X. Hao and C. Zimmer, *Nat. Biotechnol.*, 2018, **36**, 460–468.
13 P. Isola, J. Y. Zhu, T. H. Zhou and A. A. Efros, *Proc Cvpr Ieee*, 2017, pp. 5967–5976, DOI: **10.1109/Cvpr.2017.632**.
14 H. Gai, Y. Li and E. S. Yeung, *Microfluidics*, 2011, 171–201.
15 D. Măriuța, S. Colin, C. Barrot-Lattes, S. Le Calvé, J. G. Korvink, L. Baldas and J. J. Brandner, *Microfluid. Nanofluid.*, 2020, **24**, 1–28.
16 V. Boominathan, J. T. Robinson, L. Waller and A. Veeraraghavan, *Optica*, 2021, **9**, 1–16.
17 N. Nitta, T. Iino, A. Isozaki, M. Yamagishi, Y. Kitahama, S. Sakuma, Y. Suzuki, H. Tezuka, M. Oikawa, F. Arai, T. Asai, D. Deng, H. Fukuzawa, M. Hase, T. Hasunuma, T. Hayakawa, K. Hiraki, K. Hiramatsu, Y. Hoshino, M. Inaba, Y. Inoue, T. Ito, M. Kajikawa, H. Karakawa, Y. Kasai, Y. Kato, H. Kobayashi, C. Lei, S. Matsusaka, H. Mikami, A. Nakagawa, K. Numata, T. Ota, T. Sekiya, K. Shiba, Y. Shirasaki, N. Suzuki, S. Tanaka, S. Ueno, H. Watarai, T. Yamano, M. Yazawa, Y. Yonamine, D. Di Carlo, Y. Hosokawa, S. Uemura, T. Sugimura, Y. Ozeki and K. Goda, *Nat. Commun.*, 2020, **11**, 3452.
18 J. Gala de Pablo, M. Lindley, K. Hiramatsu and K. Goda, *Acc. Chem. Res.*, 2021, **54**, 2132–2143.
19 Y. Wakisaka, Y. Suzuki, O. Iwata, A. Nakashima, T. Ito, M. Hirose, R. Domon, M. Sugawara, N. Tsumura and H. Watarai, *Nat. Microbiol.*, 2016, **1**, 1–4.
20 R. Prevedel, A. Diz-Muñoz, G. Ruocco and G. Antonacci, *Nat. Methods*, 2019, **16**, 969–977.
21 J. Zhang, X. A. Nou, H. Kim and G. Scarcelli, *Lab Chip*, 2017, **17**, 663–670.
22 Y. J. Fan, H. Y. Hsieh, S. F. Tsai, C. H. Wu, C. M. Lee, Y. T. Liu, C. H. Lu, S. W. Chang and B. C. Chen, *Lab Chip*, 2021, **21**, 344–354.
23 X. Chen, J. Ping, Y. Sun, C. Yi, S. Liu, Z. Gong and P. Fei, *Lab Chip*, 2021, **21**, 3420–3428.
24 E. J. Vargas-Ordaz, S. Gorelick, H. M. York, B. Liu, M. L. Halls, S. Arumugam, A. Neild, A. de Marco and V. J. Cadarso, *Lab Chip*, 2021, **21**, 2945–2954.
25 R. Memeo, P. Paiè, F. Sala, M. Castriotta, C. Guercio, T. Vaccari, R. Osellame, A. Bassi and F. Bragheri, *J. Biophotonics*, 2021, **14**, e202000396.
26 M. Lelek, M. T. Gyparaki, G. Beliu, F. Schueder, J. Griffié, S. Manley, R. Jungmann, M. Sauer, M. Lakadamyali and C. Zimmer, *Nat. Rev. Methods Primers*, 2021, **1**, 1–27.
27 B.-C. Chen, W. R. Legant, K. Wang, L. Shao, D. E. Milkie, M. W. Davidson, C. Janetopoulos, X. S. Wu, J. A. Hammer III and Z. Liu, *Science*, 2014, **346**, 1257998.
28 A. Ahmad, F. Sala, P. Paiè, A. Candeo, S. D'Annunzio, A. Zippo, C. Frindel, R. Osellame, F. Bragheri, A. Bassi and D. Rousseau, *Lab Chip*, 2022, **22**, 3453–3463.
29 S. Dong, K. Guo, P. Nanda, R. Shiradkar and G. Zheng, *Biomed. Opt. Express*, 2014, **5**, 3305–3310.
30 J. Chung, J. Kim, X. Ou, R. Horstmeyer and C. Yang, *Biomed. Opt. Express*, 2016, **7**, 352–368.
31 L. Xu, J. S. Ren, C. Liu and J. Jia, *Advances in neural information processing systems*, 2014, vol. 27.
32 H. Zhao, Z. Ke, N. Chen, S. Wang, K. Li, L. Wang, X. Gong, W. Zheng, L. Song and Z. Liu, *J. Biophotonics*, 2020, **13**, e201960147.
33 F. Zhang, C. Lei, C. J. Huang, H. Kobayashi, C. W. Sun and K. Goda, *Cytometry, Part A*, 2019, **95**, 549–554.
34 M. Weigert, U. Schmidt, T. Boothe, A. Müller, A. Dibrov, A. Jain, B. Wilhelm, D. Schmidt, C. Broaddus and S. Culley, *Nat. Methods*, 2018, **15**, 1090–1097.
35 O. Ronneberger, P. Fischer and T. Brox, presented in part at the International Conference on Medical image computing and computer-assisted intervention, 2015.

36 J. Lehtinen, J. Munkberg, J. Hasselgren, S. Laine, T. Karras, M. Aittala and T. Aila, *arXiv*, 2018, preprint, arXiv:1803.04189, DOI: **10.48550/arXiv.1803.04189**.
37 A. Krull, T.-O. Buchholz and F. Jug, presented in part at the Proceedings of the IEEE/CVF Conference on Computer Vision and Pattern Recognition, 2019.
38 J. Batson and L. Royer, presented in part at the International Conference on Machine Learning, 2019.
39 Y. Zhang, Y. Zhu, E. Nichols, Q. Wang, S. Zhang, C. Smith and S. Howard, presented in part at the Proceedings of the IEEE/CVF Conference on Computer Vision and Pattern Recognition, 2019.
40 W. Xiao, L. Xin, R. Cao, X. Wu, R. Tian, L. Che, L. Sun, P. Ferraro and F. Pan, *Lab Chip*, 2021, **21**, 1385–1394.
41 J. Chen, H. Sasaki, H. Lai, Y. Su, J. Liu, Y. Wu, A. Zhovmer, C. A. Combs, I. Rey-Suarez and H.-Y. Chang, *Nat. Methods*, 2021, **18**, 678–687.
42 A. S. Goncharova, A. Honigmann, F. Jug and A. Krull, presented in part at the European Conference on Computer Vision, 2020.
43 T.-O. Buchholz, M. Prakash, D. Schmidt, A. Krull and F. Jug, presented in part at the European Conference on Computer Vision, 2020.
44 I. Goodfellow, J. Pouget-Abadie, M. Mirza, B. Xu, D. Warde-Farley, S. Ozair, A. Courville and Y. Bengio, *Advances in neural information processing systems*, 2014, vol. 27.
45 S. Lim, H. Park, S.-E. Lee, S. Chang, B. Sim and J. C. Ye, *IEEE Trans. Comput. Imaging*, 2020, **6**, 1127–1138.
46 Y. Wu, Y. Rivenson, H. Wang, Y. Luo, E. Ben-David, L. A. Bentolila, C. Pritz and A. Ozcan, *Nat. Methods*, 2019, **16**, 1323–1331.
47 X. Yang, L. Huang, Y. Luo, Y. Wu, H. Wang, Y. Rivenson and A. Ozcan, *ACS Photonics*, 2021, **8**, 2174–2182.
48 A. Dosovitskiy, L. Beyer, A. Kolesnikov, D. Weissenborn, X. Zhai, T. Unterthiner, M. Dehghani, M. Minderer, G. Heigold and S. Gelly, *arXiv*, 2020, preprint, arXiv:2010.11929, DOI: **10.48550/arXiv.2010.11929**.
49 C. N. Christensen, M. Lu, E. N. Ward, P. Lio and C. F. Kaminski, *arXiv*, 2022, preprint, arXiv:2203.00030, DOI: **10.48550/arXiv.2203.00030**.
50 X. Li, J. Suo, W. Zhang, X. Yuan and Q. Dai, presented in part at the Proceedings of the IEEE/CVF International Conference on Computer Vision, 2021.
51 K. Yanny, K. Monakhova, R. W. Shuai and L. Waller, *Optica*, 2022, **9**, 96–99.
52 H. Kobayashi, A. C. Solak, J. Batson and L. A. Royer, *arXiv*, 2020, preprint arXiv:2006.06156, DOI: **10.48550/arXiv.2006.06156**.
53 G. Barbastathis, A. Ozcan and G. Situ, *Optica*, 2019, **6**, 921–943.
54 G. Wang, J. C. Ye and B. De Man, *Nat. Mach. Intell.*, 2020, **2**, 737–748.
55 A. Ozcan and E. McLeod, *Annu. Rev. Biomed. Eng.*, 2016, **18**, 77–102.
56 R. S. Fischer, Y. Wu, P. Kanchanawong, H. Shroff and C. M. Waterman, *Trends Cell Biol.*, 2011, **21**, 682–691.
57 J. Wu, N. Ji and K. K. Tsia, *Nat. Photonics*, 2021, **15**, 800–812.
58 E. H. Stelzer, F. Strobl, B.-J. Chang, F. Preusser, S. Preibisch, K. McDole and R. Fiolka, *Nat. Rev. Methods Primers*, 2021, **1**, 1–25.
59 J. Wu and R. K. Chan, *Opt. Express*, 2013, **21**, 23921–23926.
60 V. K. Jagannadh, M. D. Mackenzie, P. Pal, A. K. Kar and S. S. Gorthi, *Opt. Express*, 2016, **24**, 22144–22158.
61 F. Sala, M. Castriotta, P. Paie, A. Farina, S. D'Annunzio, A. Zippo, R. Osellame, F. Bragheri and A. Bassi, *Biomed. Opt. Express*, 2020, **11**, 4397–4407.
62 Y. Han, R. Tang, Y. Gu, A. C. Zhang, W. Cai, V. Castor, S. H. Cho, W. Alaynick and Y.-H. Lo, *Optica*, 2019, **6**, 1297–1304.
63 Y. Y. Chen, P. N. Silva, A. M. Syed, S. Sindhwani, J. V. Rocheleau and W. C. Chan, *Proc. Natl. Acad. Sci. U. S. A.*, 2016, **113**, 14915–14920.
64 P. Paiè, F. Bragheri, A. Bassi and R. Osellame, *Lab Chip*, 2016, **16**, 1556–1560.
65 E. J. Gualda, H. Pereira, T. Vale, M. F. Estrada, C. Brito and N. Moreno, *Biomed. Opt. Express*, 2015, **6**, 4447–4456.
66 J. Pawley, *Handbook of biological confocal microscopy*, Springer Science & Business Media, 2006.
67 T. Kim, R. Zhou, M. Mir, S. D. Babacan, P. S. Carney, L. L. Goddard and G. Popescu, *Nat. Photonics*, 2014, **8**, 256–263.
68 Y. Sung, W. Choi, C. Fang-Yen, K. Badizadegan, R. R. Dasari and M. S. Feld, *Opt. Express*, 2009, **17**, 266–277.
69 G. Zheng, R. Horstmeyer and C. Yang, *Nat. Photonics*, 2013, **7**, 739–745.
70 S. Jiang, J. Zhu, P. Song, C. Guo, Z. Bian, R. Wang, Y. Huang, S. Wang, H. Zhang and G. Zheng, *Lab Chip*, 2020, **20**, 1058–1065.
71 R. Prevedel, Y.-G. Yoon, M. Hoffmann, N. Pak, G. Wetzstein, S. Kato, T. Schrödel, R. Raskar, M. Zimmer and E. S. Boyden, *Nat. Methods*, 2014, **11**, 727–730.
72 Z. Zhang, L. Bai, L. Cong, P. Yu, T. Zhang, W. Shi, F. Li, J. Du and K. Wang, *Nat. Biotechnol.*, 2021, **39**, 74–83.
73 Y. Park, C. Depeursinge and G. Popescu, *Nat. Photonics*, 2018, **12**, 578–589.
74 K. C. Lee, M. Wang, K. S. Cheah, G. C. Chan, H. K. So, K. K. Wong and K. K. Tsia, *Cytometry, Part A*, 2019, **95**, 510–520.
75 P. Song, C. Guo, S. Jiang, T. Wang, P. Hu, D. Hu, Z. Zhang, B. Feng and G. Zheng, *Lab Chip*, 2021, **21**, 4549–4556.
76 S. Seo, T.-W. Su, D. K. Tseng, A. Erlinger and A. Ozcan, *Lab Chip*, 2009, **9**, 777–787.
77 W. Choi, C. Fang-Yen, K. Badizadegan, S. Oh, N. Lue, R. R. Dasari and M. S. Feld, *Nat. Methods*, 2007, **4**, 717–719.
78 N. C. Pégard, M. L. Toth, M. Driscoll and J. W. Fleischer, *Lab Chip*, 2014, **14**, 4447–4450.
79 F. Merola, P. Memmolo, L. Miccio, R. Savoia, M. Mugnano, A. Fontana, G. D'ippolito, A. Sardo, A. Iolascon and A. Gambale, *Light: Sci. Appl.*, 2017, **6**, e16241.
80 Y. Rivenson, Y. Zhang, H. Günaydın, D. Teng and A. Ozcan, *Light: Sci. Appl.*, 2018, **7**, 17141–17141.
81 H. Wang, M. Lyu and G. Situ, *Opt. Express*, 2018, **26**, 22603–22614.

82 T. C. Nguyen, V. Bui and G. Nehmetallah, *Opt. Eng.*, 2018, **57**, 043111.
83 T. Nguyen, Y. Xue, Y. Li, L. Tian and G. Nehmetallah, *Opt. Express*, 2018, **26**, 26470–26484.
84 F. Wang, H. Wang, H. Wang, G. Li and G. Situ, *Opt. Express*, 2019, **27**, 25560–25572.
85 Z. Wang, L. Zhu, H. Zhang, G. Li, C. Yi, Y. Li, Y. Yang, Y. Ding, M. Zhen and S. Gao, *Nat. Methods*, 2021, **18**, 551–556.
86 J. Wu, L. Cao and G. Barbastathis, *Opt. Lett.*, 2021, **46**, 130–133.
87 N. Wagner, F. Beuttenmueller, N. Norlin, J. Gierten, J. C. Boffi, J. Wittbrodt, M. Weigert, L. Hufnagel, R. Prevedel and A. Kreshuk, *Nat. Methods*, 2021, **18**, 557–563.
88 K. C. Zhou and R. Horstmeyer, *Opt. Express*, 2020, **28**, 12872–12896.
89 A. Speiser, L.-R. Müller, P. Hoess, U. Matti, C. J. Obara, W. R. Legant, A. Kreshuk, J. H. Macke, J. Ries and S. C. Turaga, *Nat. Methods*, 2021, **18**, 1082–1090.
90 C. Qiao, D. Li, Y. Guo, C. Liu, T. Jiang, Q. Dai and D. Li, *Nat. Methods*, 2021, **18**, 194–202.
91 F. Yang, T.-A. Pham, H. Gupta, M. Unser and J. Ma, *Opt. Express*, 2020, **28**, 3905–3921.
92 A. Goy, G. Rughoobur, S. Li, K. Arthur, A. I. Akinwande and G. Barbastathis, *Proc. Natl. Acad. Sci. U. S. A.*, 2019, **116**, 19848–19856.
93 S. Li, M. Deng, J. Lee, A. Sinha and G. Barbastathis, *Optica*, 2018, **5**, 803–813.
94 D. Ulyanov, A. Vedaldi and V. Lempitsky, presented in part at the Proceedings of the IEEE conference on computer vision and pattern recognition, 2018.
95 F. Wang, Y. Bian, H. Wang, M. Lyu, G. Pedrini, W. Osten, G. Barbastathis and G. Situ, *Light: Sci. Appl.*, 2020, **9**, 1–7.
96 U. S. Kamilov, I. N. Papadopoulos, M. H. Shoreh, A. Goy, C. Vonesch, M. Unser and D. Psaltis, *Optica*, 2015, **2**, 517–522.
97 K. C. Gwosch, J. K. Pape, F. Balzarotti, P. Hoess, J. Ellenberg, J. Ries and S. W. Hell, *Nat. Methods*, 2020, **17**, 217–224.
98 Z. Liu, L. D. Lavis and E. Betzig, *Mol. Cell*, 2015, **58**, 644–659.
99 G. Jacquemet, A. F. Carisey, H. Hamidi, R. Henriques and C. Leterrier, *J. Cell Sci.*, 2020, **133**, jcs240713.
100 J. Valli, A. Garcia-Burgos, L. M. Rooney, B. V. D. M. e Oliveira, R. R. Duncan and C. Rickman, *J. Biol. Chem.*, 2021, **297**, 100971.
101 W. Bishara, T.-W. Su, A. F. Coskun and A. Ozcan, *Opt. Express*, 2010, **18**, 11181–11191.
102 A. Chan, H.-C. Ng, S. C. Bogaraju, H. K. So, E. Y. Lam and K. K. Tsia, *Sci. Rep.*, 2017, **7**, 1–11.
103 S. Jiang, C. Guo, P. Song, N. Zhou, Z. Bian, J. Zhu, R. Wang, P. Dong, Z. Zhang and J. Liao, *ACS Photonics*, 2021, **8**, 3261–3271.
104 S. Jiang, C. Guo, P. Song, T. Wang, R. Wang, T. Zhang, Q. Wu, R. Pandey and G. Zheng, *Lab Chip*, 2022, **22**, 2657–2670.
105 S. Jiang, C. Guo, T. Wang, J. Liu, P. Song, T. Zhang, R. Wang, B. Feng and G. Zheng, *ACS Sens.*, 2022, **7**, 1058–1067.
106 E. Betzig, G. H. Patterson, R. Sougrat, O. W. Lindwasser, S. Olenych, J. S. Bonifacino, M. W. Davidson, J. Lippincott-Schwartz and H. F. Hess, *Science*, 2006, **313**, 1642–1645.
107 M. J. Rust, M. Bates and X. Zhuang, *Nat. Methods*, 2006, **3**, 793–796.
108 S. Stallinga and B. Rieger, *Opt. Express*, 2010, **18**, 24461–24476.
109 S. R. P. Pavani, M. A. Thompson, J. S. Biteen, S. J. Lord, N. Liu, R. J. Twieg, R. Piestun and W. E. Moerner, *Proc. Natl. Acad. Sci. U. S. A.*, 2009, **106**, 2995–2999.
110 Y. Shechtman, L. E. Weiss, A. S. Backer, S. J. Sahl and W. Moerner, *Nano Lett.*, 2015, **15**, 4194–4199.
111 E. Nehme, L. E. Weiss, T. Michaeli and Y. Shechtman, *Optica*, 2018, **5**, 458–464.
112 E. Nehme, D. Freedman, R. Gordon, B. Ferdman, L. E. Weiss, O. Alalouf, T. Naor, R. Orange, T. Michaeli and Y. Shechtman, *Nat. Methods*, 2020, **17**, 734–740.
113 N. Boyd, E. Jonas, H. Babcock and B. Recht, *BioRxiv*, 2018, preprint, 267096, DOI: **10.1101/267096**.
114 P. Zelger, K. Kaser, B. Rossboth, L. Velas, G. Schütz and A. Jesacher, *Opt. Express*, 2018, **26**, 33166–33179.
115 H. Ma, J. Xu and Y. Liu, *Sci. Adv.*, 2019, **5**, eaaw0683.
116 B. Al Alwan, K. AbuZineh, S. Nozue, A. Rakhmatulina, M. Aldehaiman, A. S. Al-Amoodi, M. F. Serag, F. A. Aleisa, J. S. Merzaban and S. Habuchi, *Commun. Biol.*, 2021, **4**, 1–14.
117 J. Tam, G. A. Cordier, Š. Bálint, Á. Sandoval Álvarez, J. S. Borbely and M. Lakadamyali, *PLoS One*, 2014, **9**, e115512.
118 D. I. Cattoni, J.-B. Fiche, A. Valeri, T. Mignot and M. Nöllmann, *PLoS One*, 2013, **8**, e76268.
119 H. Wang, Y. Rivenson, Y. Jin, Z. Wei, R. Gao, H. Günaydın, L. A. Bentolila, C. Kural and A. Ozcan, *Nat. Methods*, 2019, **16**, 103–110.
120 K. Huang, H. Matsumura, Y. Zhao, M. Herbig, D. Yuan, Y. Mineharu, J. Harmon, J. Findinier, M. Yamagishi and S. Ohnuki, *Lab Chip*, 2022, **22**, 876–889.
121 H. Zhang, Y. Zhao, C. Fang, G. Li, M. Zhang, Y.-H. Zhang and P. Fei, *Optica*, 2020, **7**, 1627–1640.
122 H. Zhang, C. Fang, X. Xie, Y. Yang, W. Mei, D. Jin and P. Fei, *Biomed. Opt. Express*, 2019, **10**, 1044–1063.
123 N. Gustafsson, S. Culley, G. Ashdown, D. M. Owen, P. M. Pereira and R. Henriques, *Nat. Commun.*, 2016, **7**, 1–9.
124 C. Ounkomol, S. Seshamani, M. M. Maleckar, F. Collman and G. R. Johnson, *Nat. Methods*, 2018, **15**, 917–920.
125 E. M. Christiansen, S. J. Yang, D. M. Ando, A. Javaherian, G. Skibinski, S. Lipnick, E. Mount, A. O'neil, K. Shah and A. K. Lee, *Cell*, 2018, **173**, 792–803.e719.
126 H.-S. Liu, M.-S. Jan, C.-K. Chou, P.-H. Chen and N.-J. Ke, *Biochem. Biophys. Res. Commun.*, 1999, **260**, 712–717.
127 O. Agbulut, C. Coirault, N. Niederländer, A. Huet, P. Vicart, A. Hagège, M. Puceat and P. Menasche, *Nat. Methods*, 2006, **3**, 331–331.
128 R. Dixit and R. Cyr, *Plant J.*, 2003, **36**, 280–290.
129 M. Baens, H. Noels, V. Broeckx, S. Hagens, S. Fevery, A. D. Billiau, H. Vankelecom and P. Marynen, *PLoS One*, 2006, **1**, e54.
130 H. Yan, Y. Wu, Y. Zhou, M. Xu, P. Paiè, C. Lei, S. Yan and K. Goda, *APL Photonics*, 2020, **5**, 046103.

131 Y. Rivenson, T. Liu, Z. Wei, Y. Zhang, K. de Haan and A. Ozcan, *Light: Sci. Appl.*, 2019, **8**, 1–11.
132 S. Cheng, S. Fu, Y. M. Kim, W. Song, Y. Li, Y. Xue, J. Yi and L. Tian, *Sci. Adv.*, 2021, **7**, eabe0431.
133 S.-M. Guo, L.-H. Yeh, J. Folkesson, I. E. Ivanov, A. P. Krishnan, M. G. Keefe, E. Hashemi, D. Shin, B. B. Chhun and N. H. Cho, *eLife*, 2020, **9**, e55502.
134 M. E. Kandel, Y. R. He, Y. J. Lee, T. H.-Y. Chen, K. M. Sullivan, O. Aydin, M. T. A. Saif, H. Kong, N. Sobh and G. Popescu, *Nat. Commun.*, 2020, **11**, 1–10.
135 Y. Jo, H. Cho, W. S. Park, G. Kim, D. Ryu, Y. S. Kim, M. Lee, S. Park, M. J. Lee and H. Joo, *Nat. Cell Biol.*, 2021, 1329–1337.
136 Y. Zhang, L. Kang, I. H. Wong, W. Dai, X. Li, R. C. Chan, M. K. Hsin and T. T. Wong, *Adv. Sci.*, 2022, **9**, 2102358.
137 A. M. White, Y. Zhang, J. G. Shamul, J. Xu, E. A. Kwizera, B. Jiang and X. He, *Small*, 2021, **17**, e2100491.
138 O. M. O'Connor, R. N. Alnahhas, J. B. Lugagne and M. J. Dunlop, *PLoS Comput. Biol.*, 2022, **18**, e1009797.
139 Y. Song, J. Zhao, T. Cai, A. Stephens, S. H. Su, E. Sandford, C. Flora, B. H. Singer, M. Ghosh, S. W. Choi, M. Tewari and K. Kurabayashi, *Biosens. Bioelectron.*, 2021, **180**, 113088.
140 M. A. Sami, M. Tayyab, P. Parikh, H. Govindaraju and U. Hassan, *Analyst*, 2021, **146**, 2531–2541.
141 R. Zenhausern, A. S. Day, B. Safavinia, S. Han, P. E. Rudy, Y. W. Won and J. Y. Yoon, *Biosens. Bioelectron.*, 2022, **200**, 113916.
142 D. Stallmann, J. P. Gopfert, J. Schmitz, A. Grunberger and B. Hammer, *Bioinformatics*, 2021, **37**(20), 3632–3639.
143 N. Praljak, S. Iram, U. Goreke, G. Singh, A. Hill, U. A. Gurkan and M. Hinczewski, *PLoS Comput. Biol.*, 2021, **17**, e1008946.
144 J. C. Caicedo, A. Goodman, K. W. Karhohs, B. A. Cimini, J. Ackerman, M. Haghighi, C. Heng, T. Becker, M. Doan, C. McQuin, M. Rohban, S. Singh and A. E. Carpenter, *Nat. Methods*, 2019, **16**, 1247–1253.
145 J. C. Caicedo, J. Roth, A. Goodman, T. Becker, K. W. Karhohs, M. Broisin, C. Molnar, C. McQuin, S. Singh, F. J. Theis and A. E. Carpenter, *Cytometry, Part A*, 2019, **95**, 952–965.
146 R. Hollandi, A. Szkalisity, T. Toth, E. Tasnadi, C. Molnar, B. Mathe, I. Grexa, J. Molnar, A. Balind and M. Gorbe, *Cell Syst.*, 2020, **10**, 453–458.e456.
147 D. A. Van Valen, T. Kudo, K. M. Lane, D. N. Macklin, N. T. Quach, M. M. DeFelice, I. Maayan, Y. Tanouchi, E. A. Ashley and M. W. Covert, *PLoS Comput. Biol.*, 2016, **12**, e1005177.
148 T. Prangemeier, C. Wildner, A. O. Francani, C. Reich and H. Koeppl, *BioSystems*, 2022, **211**, 104557.
149 J. B. Lugagne, H. Lin and M. J. Dunlop, *PLoS Comput. Biol.*, 2020, **16**, e1007673.
150 T. Deng, D. DePaoli, L. Begin, N. Jia, L. Torres de Oliveira, D. C. Cote, W. F. Vincent and J. Greener, *Anal. Chem.*, 2021, **93**(25), 8764–8773.
151 Z. Lei, D. Xie, M. K. Mbogba, Z. Chen, C. Tian, L. Xu and G. Zhao, *Lab Chip*, 2019, **19**, 1929–1940.
152 T. Falk, D. Mai, R. Bensch, O. Cicek, A. Abdulkadir, Y. Marrakchi, A. Bohm, J. Deubner, Z. Jackel, K. Seiwald, A. Dovzhenko, O. Tietz, C. Dal Bosco, S. Walsh, D. Saltukoglu, T. L. Tay, M. Prinz, K. Palme, M. Simons, I. Diester, T. Brox and O. Ronneberger, *Nat. Methods*, 2019, **16**, 67–70.
153 C. Stringer, T. Wang, M. Michaelos and M. Pachitariu, *Nat. Methods*, 2021, **18**, 100–106.
154 U. Schmidt, M. Weigert, C. Broaddus and G. Myers, presented in part at the International Conference on Medical Image Computing and Computer-Assisted Intervention, 2018.
155 M. Schwendy, R. E. Unger and S. H. Parekh, *Bioinformatics*, 2020, **36**, 3863–3870.
156 *Human Protein Atlas*, **https://www.proteinatlas.org**.
157 *Broad Bioimage Benchmark Collection*, **https://bbbc.broadinstitute.org**.
158 *2018 Data Science Bowl*, **https://www.kaggle.com/c/data-science-bowl-2018**.
159 C. Edlund, T. R. Jackson, N. Khalid, N. Bevan, T. Dale, A. Dengel, S. Ahmed, J. Trygg and R. Sjogren, *Nat. Methods*, 2021, **18**, 1038–1045.
160 S. Berg, D. Kutra, T. Kroeger, C. N. Straehle, B. X. Kausler, C. Haubold, M. Schiegg, J. Ales, T. Beier, M. Rudy, K. Eren, J. I. Cervantes, B. Xu, F. Beuttenmueller, A. Wolny, C. Zhang, U. Koethe, F. A. Hamprecht and A. Kreshuk, *Nat. Methods*, 2019, **16**, 1226–1232.
161 L. von Chamier, R. F. Laine, J. Jukkala, C. Spahn, D. Krentzel, E. Nehme, M. Lerche, S. Hernández-Pérez, P. K. Mattila and E. Karinou, *Nat. Commun.*, 2021, **12**, 1–18.
162 M. G. Haberl, C. Churas, L. Tindall, D. Boassa, S. Phan, E. A. Bushong, M. Madany, R. Akay, T. J. Deerinck and S. T. Peltier, *Nat. Methods*, 2018, **15**, 677–680.
163 Y. Mao and Z. Yin, presented in part at the International Conference on Medical Image Computing and Computer-Assisted Intervention, 2016.
164 J. C. Kimmel, A. Y. Chang, A. S. Brack and W. F. Marshall, *PLoS Comput. Biol.*, 2018, **14**, e1005927.
165 D. Ershov, M.-S. Phan, J. W. Pylvänäinen, S. U. Rigaud, L. Le Blanc, A. Charles-Orszag, J. R. Conway, R. F. Laine, N. H. Roy and D. Bonazzi, *Nat. Methods*, 2022, 1–4.
166 M. Lawson and J. Elf, *Nat. Methods*, 2021, **18**, 358–365.
167 S. Ziegler, S. Sievers and H. Waldmann, *Cell Chem. Biol.*, 2021, **28**, 300–319.
168 P. H. Wu, D. M. Gilkes, J. M. Phillip, A. Narkar, T. W. Cheng, J. Marchand, M. H. Lee, R. Li and D. Wirtz, *Sci. Adv.*, 2020, **6**, eaaw6938.
169 J. C. Caicedo, S. Cooper, F. Heigwer, S. Warchal, P. Qiu, C. Molnar, A. S. Vasilevich, J. D. Barry, H. S. Bansal, O. Kraus, M. Wawer, L. Paavolainen, M. D. Herrmann, M. Rohban, J. Hung, H. Hennig, J. Concannon, I. Smith, P. A. Clemons, S. Singh, P. Rees, P. Horvath, R. G. Linington and A. E. Carpenter, *Nat. Methods*, 2017, **14**, 849–863.

170 Z. Wu, B. B. Chhun, G. Popova, S.-M. Guo, C. N. Kim, L.-H. Yeh, T. Nowakowski, J. Zou and S. B. Mehta, *Mol. Biol. Cell*, 2022, **33**(6), 59.
171 Y. Zhou, A. Yasumoto, C. Lei, C. J. Huang, H. Kobayashi, Y. Wu, S. Yan, C. W. Sun, Y. Yatomi and K. Goda, *eLife*, 2020, **9**, e52938.
172 A. Zaritsky, A. R. Jamieson, E. S. Welf, A. Nevarez, J. Cillay, U. Eskiocak, B. L. Cantarel and G. Danuser, *Cell Syst.*, 2021, **12**, 733–747.e736.
173 P. Eulenberg, N. Kohler, T. Blasi, A. Filby, A. E. Carpenter, P. Rees, F. J. Theis and F. A. Wolf, *Nat. Commun.*, 2017, **8**, 463.
174 V. Ayyappan, A. Chang, C. Zhang, S. K. Paidi, R. Bordett, T. Liang, I. Barman and R. Pandey, *ACS Sens.*, 2020, **5**, 3281–3289.
175 M. Doan, J. A. Sebastian, J. C. Caicedo, S. Siegert, A. Roch, T. R. Turner, O. Mykhailova, R. N. Pinto, C. McQuin, A. Goodman, M. J. Parsons, O. Wolkenhauer, H. Hennig, S. Singh, A. Wilson, J. P. Acker, P. Rees, M. C. Kolios and A. E. Carpenter, *Proc. Natl. Acad. Sci. U. S. A.*, 2020, **117**, 21381–21390.
176 Y. Suzuki, K. Kobayashi, Y. Wakisaka, D. Deng, S. Tanaka, C. J. Huang, C. Lei, C. W. Sun, H. Liu, Y. Fujiwaki, S. Lee, A. Isozaki, Y. Kasai, T. Hayakawa, S. Sakuma, F. Arai, K. Koizumi, H. Tezuka, M. Inaba, K. Hiraki, T. Ito, M. Hase, S. Matsusaka, K. Shiba, K. Suga, M. Nishikawa, M. Jona, Y. Yatomi, Y. Yalikun, Y. Tanaka, T. Sugimura, N. Nitta, K. Goda and Y. Ozeki, *Proc. Natl. Acad. Sci. U. S. A.*, 2019, **116**, 15842–15848.
177 P. H. Wu, J. M. Phillip, S. B. Khatau, W. C. Chen, J. Stirman, S. Rosseel, K. Tschudi, J. Van Patten, M. Wong, S. Gupta, A. S. Baras, J. T. Leek, A. Maitra and D. Wirtz, *Sci. Rep.*, 2015, **5**, 18437.
178 G. Pegoraro and T. Misteli, *Trends Genet.*, 2017, **33**, 604–615.
179 G. P. Way, M. Kost-Alimova, T. Shibue, W. F. Harrington, S. Gill, F. Piccioni, T. Becker, H. Shafqat-Abbasi, W. C. Hahn and A. E. Carpenter, *Mol. Biol. Cell*, 2021, **32**, 995–1005.
180 J. Nyffeler, C. Willis, R. Lougee, A. Richard, K. Paul-Friedman and J. A. Harrill, *Toxicol. Appl. Pharmacol.*, 2020, **389**, 114876.
181 C. Kandaswamy, L. M. Silva, L. A. Alexandre and J. M. Santos, *J. Biomol. Screening*, 2016, **21**, 252–259.
182 R. A. Marklein, M. W. Klinker, K. A. Drake, H. G. Polikowsky, E. C. Lessey-Morillon and S. R. Bauer, *Cytotherapy*, 2019, **21**, 17–31.
183 S. V. Stassen, G. G. Yip, K. K. Wong, J. W. Ho and K. K. Tsia, *Nat. Commun.*, 2021, **12**, 1–18.
184 K. A. Gerbin, T. Grancharova, R. M. Donovan-Maiye, M. C. Hendershott, H. G. Anderson, J. M. Brown, J. Chen, S. Q. Dinh, J. L. Gehring and G. R. Johnson, *Cell Syst.*, 2021, **12**, 670–687.e610.
185 G. Wang, S. M. Björk, M. Huang, Q. Liu, K. Campbell, J. Nielsen, H. N. Joensson and D. Petranovic, *Proc. Natl. Acad. Sci. U. S. A.*, 2019, **116**, 9324–9332.
186 A. Ramachandran, D. A. Huyke, E. Sharma, M. K. Sahoo, C. Huang, N. Banaei, B. A. Pinsky and J. G. Santiago, *Proc. Natl. Acad. Sci. U. S. A.*, 2020, **117**, 29518–29525.
187 D. Peleg-Chen, G. Shuvali, L. Brio, A. Ifrach, O. Iancu, E. Barbiro-Michaely, A. Hendel and D. Gerber, *New Biotechnol.*, 2022, **68**, 1–8.
188 D. Feldman, A. Singh, J. L. Schmid-Burgk, R. J. Carlson, A. Mezger, A. J. Garrity, F. Zhang and P. C. Blainey, *Cell*, 2019, **179**, 787–799.e717.
189 X. Yan, N. Stuurman, S. A. Ribeiro, M. E. Tanenbaum, M. A. Horlbeck, C. R. Liem, M. Jost, J. S. Weissman and R. D. Vale, *J. Cell Biol.*, 2021, **220**, e202008158.
190 Y. Jiao, U. Ahmed, M. M. Sim, A. Bejar, X. Zhang, M. M. U. Talukder, R. Rice, J. Flannick, A. I. Podgornaia and D. F. Reilly, *Mol. Metab.*, 2019, **24**, 108–119.
191 P. Rosendahl, K. Plak, A. Jacobi, M. Kraeter, N. Toepfner, O. Otto, C. Herold, M. Winzi, M. Herbig, Y. Ge, S. Girardo, K. Wagner, B. Baum and J. Guck, *Nat. Methods*, 2018, **15**, 355–358.
192 M. Doan, C. Barnes, C. McQuin, J. C. Caicedo, A. Goodman, A. E. Carpenter and P. Rees, *Nat. Protoc.*, 2021, **16**, 3572–3595.
193 D. Di Carlo, D. Irimia, R. G. Tompkins and M. Toner, *Proc. Natl. Acad. Sci. U. S. A.*, 2007, **104**, 18892–18897.
194 D. Di Carlo, *Lab Chip*, 2009, **9**, 3038–3046.
195 X. Xuan, J. Zhu and C. Church, *Microfluid. Nanofluid.*, 2010, **9**, 1–16.
196 S. Stavrakis, G. Holzner, J. Choo and A. DeMello, *Curr. Opin. Biotechnol.*, 2019, **55**, 36–43.
197 A. Hirotsu, H. Kikuchi, H. Yamada, Y. Ozaki, R. Haneda, S. Kawata, T. Murakami, T. Matsumoto, Y. Hiramatsu, K. Kamiya, D. Yamashita, Y. Fujimori, Y. Ueda, S. Okazaki, M. Kitagawa, H. Konno and H. Takeuchi, *Lab Chip*, 2022, **22**, 3464–3474.
198 S. K. Paidi, P. Raj, R. Bordett, C. Zhang, S. H. Karandikar, R. Pandey and I. Barman, *Biosens. Bioelectron.*, 2021, **190**, 113403.
199 R. Tang, Z. Zhang, X. Chen, L. Waller, A. C. Zhang, J. Chen, Y. Han, C. An, S. H. Cho and Y.-H. Lo, *APL Photonics*, 2020, **5**, 126105.
200 J. Sun, L. Wang, Q. Liu, A. Tarnok and X. Su, *Biomed. Opt. Express*, 2020, **11**, 6674–6686.
201 H. S. Park, H. Price, S. Ceballos, J. T. Chi and A. Wax, *Cell*, 2021, **10**, 2455.
202 W. Zhao, Y. Guo, S. Yang, M. Chen and H. Chen, *J. Biomed. Opt.*, 2020, **25**, 1–12.
203 Y. Wu, Y. Zhou, C. J. Huang, H. Kobayashi, S. Yan, Y. Ozeki, Y. Wu, C. W. Sun, A. Yasumoto, Y. Yatomi, C. Lei and K. Goda, *Opt. Express*, 2020, **28**, 519–532.
204 N. Nissim, M. Dudaie, I. Barnea and N. T. Shaked, *Cytometry, Part A*, 2021, **99**, 511–523.
205 M. Herbig, A. Jacobi, M. Wobus, H. Weidner, A. Mies, M. Krater, O. Otto, C. Thiede, M. T. Weickert, K. S. Gotze, M. Rauner, L. C. Hofbauer, M. Bornhauser, J. Guck, M. Ader, U. Platzbecker and E. Balaian, *Sci. Rep.*, 2022, **12**, 870.

206 V. Rizzuto, A. Mencattini, B. Alvarez-Gonzalez, D. Di Giuseppe, E. Martinelli, D. Beneitez-Pastor, M. D. M. Manu-Pereira, M. J. Lopez-Martinez and J. Samitier, *Sci. Rep.*, 2021, **11**, 13553.
207 E. S. Lamoureux, E. Islamzada, M. V. J. Wiens, K. Matthews, S. P. Duffy and H. Ma, *Lab Chip*, 2021, **22**, 26–39.
208 J. Guck, S. Schinkinger, B. Lincoln, F. Wottawah, S. Ebert, M. Romeyke, D. Lenz, H. M. Erickson, R. Ananthakrishnan and D. Mitchell, *Biophys. J.*, 2005, **88**, 3689–3698.
209 P.-H. Wu, D. R.-B. Aroush, A. Asnacios, W.-C. Chen, M. E. Dokukin, B. L. Doss, P. Durand-Smet, A. Ekpenyong, J. Guck and N. V. Guz, *Nat. Methods*, 2018, **15**, 491–498.
210 C. Petchakup, H. Yang, L. Gong, L. He, H. M. Tay, R. Dalan, A. J. Chung, K. H. H. Li and H. W. Hou, *Small*, 2022, 2104822.
211 M. DaOrazio, R. Reale, A. De Ninno, M. A. Brighetti, A. Mencattini, L. Businaro, E. Martinelli, P. Bisegna, A. Travaglini and F. Caselli, *IEEE Trans. Biomed. Eng.*, 2022, **69**, 921–931.
212 H. Hashemzadeh, S. Shojaeilangari, A. Allahverdi, M. Rothbauer, P. Ertl and H. Naderi-Manesh, *Sci. Rep.*, 2021, **11**, 9804.
213 A. Mencattini, D. Di Giuseppe, M. C. Comes, P. Casti, F. Corsi, F. R. Bertani, L. Ghibelli, L. Businaro, C. Di Natale, M. C. Parrini and E. Martinelli, *Sci. Rep.*, 2020, **10**, 7653.
214 Z. Zhang, L. Chen, Y. Wang, T. Zhang, Y. C. Chen and E. Yoon, *Anal. Chem.*, 2019, **91**, 14093–14100.
215 Y. C. Chen, Z. Zhang and E. Yoon, *Anal. Chem.*, 2020, **92**, 7717–7724.
216 M. Perez-Aliacar, M. H. Doweidar, M. Doblare and J. Ayensa-Jimenez, *Comput. Biol. Med.*, 2021, **135**, 104547.
217 C. R. Oliver, T. M. Westerhof, M. G. Castro and S. D. Merajver, *J. Visualized Exp.*, 2020, e61654.
218 M. Ghafari, J. Clark, H. B. Guo, R. Yu, Y. Sun, W. Dang and H. Qin, *PLoS One*, 2021, **16**, e0246988.
219 S. Mondal, E. Hegarty, C. Martin, S. K. Gökçe, N. Ghorashian and A. Ben-Yakar, *Nat. Commun.*, 2016, **7**, 1–11.
220 A. Isozaki, J. Harmon, Y. Zhou, S. Li, Y. Nakagawa, M. Hayashi, H. Mikami, C. Lei and K. Goda, *Lab Chip*, 2020, **20**, 3074–3090.
221 J. Riordon, D. Sovilj, S. Sanner, D. Sinton and E. W. K. Young, *Trends Biotechnol.*, 2019, **37**, 310–324.
222 M. M. Waldrop, *Nature*, 2015, **518**, 20.
223 K. M. Hampson, R. Turcotte, D. T. Miller, K. Kurokawa, J. R. Males, N. Ji and M. J. Booth, *Nat. Rev. Methods Primers*, 2021, **1**, 68.
224 L. A. Royer, W. C. Lemon, R. K. Chhetri, Y. Wan, M. Coleman, E. W. Myers and P. J. Keller, *Nat. Biotechnol.*, 2016, **34**, 1267–1278.
225 J. He and J. Huisken, *Nat. Commun.*, 2020, **11**, 1–9.
226 A. Durand, T. Wiesner, M.-A. Gardner, L.-É. Robitaille, A. Bilodeau, C. Gagné, P. De Koninck and F. Lavoie-Cardinal, *Nat. Commun.*, 2018, **9**, 1–16.
227 M. Štefko, B. Ottino, K. M. Douglass and S. Manley, *Opt. Express*, 2018, **26**, 30882–30900.
228 O. J. Dressler, P. D. Howes, J. Choo and A. J. deMello, *ACS Omega*, 2018, **3**, 10084–10091.
229 A. Chu, D. Nguyen, S. S. Talathi, A. C. Wilson, C. Ye, W. L. Smith, A. D. Kaplan, E. B. Duoss, J. K. Stolaroff and B. Giera, *Lab Chip*, 2019, **19**, 1808–1817.
230 J. W. Khor, N. Jean, E. S. Luxenberg, S. Ermon and S. K. Y. Tang, *Soft Matter*, 2019, **15**, 1361–1372.
231 Z. Zhou, X. Li and R. N. Zare, *ACS Cent. Sci.*, 2017, **3**, 1337–1344.
232 B. A. Rizkin, A. S. Shkolnik, N. J. Ferraro and R. L. Hartman, *Nat. Mach. Intell.*, 2020, **2**, 200–209.
233 Y. Zhao, Y. Cheng, L. Shang, J. Wang, Z. Xie and Z. Gu, *Small*, 2015, **11**, 151–174.
234 A. Isozaki, H. Mikami, H. Tezuka, H. Matsumura, K. Huang, M. Akamine, K. Hiramatsu, T. Iino, T. Ito, H. Karakawa, Y. Kasai, Y. Li, Y. Nakagawa, S. Ohnuki, T. Ota, Y. Qian, S. Sakuma, T. Sekiya, Y. Shirasaki, N. Suzuki, E. Tayyabi, T. Wakamiya, M. Xu, M. Yamagishi, H. Yan, Q. Yu, S. Yan, D. Yuan, W. Zhang, Y. Zhao, F. Arai, R. E. Campbell, C. Danelon, D. Di Carlo, K. Hiraki, Y. Hoshino, Y. Hosokawa, M. Inaba, A. Nakagawa, Y. Ohya, M. Oikawa, S. Uemura, Y. Ozeki, T. Sugimura, N. Nitta and K. Goda, *Lab Chip*, 2020, **20**, 2263–2273.
235 D. Schraivogel, T. M. Kuhn, B. Rauscher, M. Rodríguez-Martínez, M. Paulsen, K. Owsley, A. Middlebrook, C. Tischer, B. Ramasz and D. Ordoñez-Rueda, *Science*, 2022, **375**, 315–320.
236 X. Chen, Y. Gu, J. Chen, C.-H. Lee, I. Gagne, R. Tang, L. Waller, Z. Zhang, A. C. Zhang and Y. Han, *APL Photonics*, 2020, **5**, 040801.
237 A. A. Nawaz, M. Urbanska, M. Herbig, M. Notzel, M. Krater, P. Rosendahl, C. Herold, N. Toepfner, M. Kubankova, R. Goswami, S. Abuhattum, F. Reichel, P. Muller, A. Taubenberger, S. Girardo, A. Jacobi and J. Guck, *Nat. Methods*, 2020, **17**, 595–599.
238 Y. Gu, A. C. Zhang, Y. Han, J. Li, C. Chen and Y. H. Lo, *Cytometry, Part A*, 2019, **95**, 499–509.
239 K. Lee, S. E. Kim, J. Doh, K. Kim and W. K. Chung, *Lab Chip*, 2021, **21**, 1798–1810.
240 P. Almada, P. M. Pereira, S. Culley, G. Caillol, F. Boroni-Rueda, C. L. Dix, G. Charras, B. Baum, R. F. Laine and C. Leterrier, *Nat. Commun.*, 2019, **10**, 1–9.
241 C. D. Edington, W. L. K. Chen, E. Geishecker, T. Kassis, L. R. Soenksen, B. M. Bhushan, D. Freake, J. Kirschner, C. Maass and N. Tsamandouras, *Sci. Rep.*, 2018, **8**, 1–18.
242 S. E. Park, A. Georgescu and D. Huh, *Science*, 2019, **364**, 960–965.
243 H. Clevers, *Cell*, 2016, **165**, 1586–1597.
244 B. Schuster, M. Junkin, S. S. Kashaf, I. Romero-Calvo, K. Kirby, J. Matthews, C. R. Weber, A. Rzhetsky, K. P. White and S. Tay, *Nat. Commun.*, 2020, **11**, 1–12.
245 L. Broutier, G. Mastrogiovanni, M. Verstegen, H. E. Francies, L. M. Gavarró, C. R. Bradshaw, G. E. Allen, R. Arnes-Benito, O. Sidorova and M. P. Gaspersz, *Nat. Med.*, 2017, **23**, 1424–1435.

246 Y. S. Zhang, J. Aleman, S. R. Shin, T. Kilic, D. Kim, S. A. Mousavi Shaegh, S. Massa, R. Riahi, S. Chae and N. Hu, *Proc. Natl. Acad. Sci. U. S. A.*, 2017, **114**, E2293–E2302.
247 H. Cai, Z. Ao, Z. Wu, S. Song, K. Mackie and F. Guo, *Lab Chip*, 2021, **21**, 2194–2205.
248 S. N. Ooft, F. Weeber, K. K. Dijkstra, C. M. McLean, S. Kaing, E. van Werkhoven, L. Schipper, L. Hoes, D. J. Vis and J. van de Haar, *Sci. Transl. Med.*, 2019, **11**, eaay2574.
249 R. Perrault, Y. Shoham, E. Brynjolfsson, J. Clark, J. Etchemendy, B. Grosz, T. Lyons, J. Manyika, S. Mishra and J. C. Niebles, *The AI index 2019 annual report*, AI Index Steering Committee, Human-Centered AI Institute, Stanford University, Stanford, CA, 2019.
250 N. P. Jouppi, C. Young, N. Patil, D. Patterson, G. Agrawal, R. Bajwa, S. Bates, S. Bhatia, N. Boden and A. Borchers, presented in part at the Proceedings of the 44th annual international symposium on computer architecture, 2017.
251 K. Guo, S. Zeng, J. Yu, Y. Wang and H. Yang, *ACM Trans. Reconfigurable Technol. Syst.*, 2019, **12**, 1–26.
252 N. Nitta, T. Sugimura, A. Isozaki, H. Mikami, K. Hiraki, S. Sakuma, T. Iino, F. Arai, T. Endo and Y. Fujiwaki, *Cell*, 2018, **175**, 266–276.e213.
253 M. Wang, K. C. Lee, B. M. Chung, S. V. Bogaraju, H.-C. Ng, J. S. Wong, H. C. Shum, K. K. Tsia and H. K.-H. So, *IEEE Trans. Neural Netw. Learn. Syst.*, 2021, 2853–2866.
254 S. I. Venieris and C.-S. Bouganis, presented in part at the 2017 27th International Conference on Field Programmable Logic and Applications (FPL), 2017.
255 Y. Liao, N. Yu, D. Tian, S. Li and Z. Li, *Sensors*, 2019, **19**, 5103.
256 W. Ouyang, F. Mueller, M. Hjelmare, E. Lundberg and C. Zimmer, *Nat. Methods*, 2019, **16**, 1199–1200.
257 *Cell Image Library*, **https://www.cellimagelibrary.org/**.
258 *Image Data Resource*, **https://idr.openmicroscopy.org/**.
259 *RxRx library*, **https://www.rxrx.ai/**.
260 E. Williams, J. Moore, S. W. Li, G. Rustici, A. Tarkowska, A. Chessel, S. Leo, B. Antal, R. K. Ferguson, U. Sarkans, A. Brazma, R. E. C. Salas and J. R. Swedlow, *Nat. Methods*, 2017, **14**, 775–781.
261 C. D. Schuman, S. R. Kulkarni, M. Parsa, J. P. Mitchell, P. Date and B. Kay, *Nat. Comput. Sci.*, 2022, **2**, 10–19.